HHS Public Access

Author manuscript

Cell. Author manuscript; available in PMC 2021 December 23.

Published in final edited form as:

Cell. 2020 December 23; 183(7): 1813–1825.e18. doi:10.1016/j.cell.2020.11.014.

How GPCR phosphorylation patterns orchestrate arrestin-mediated signaling

Naomi R. Latorraca[1,2,3,4,5,7,10], **Matthieu Masureel**[3,8,10,*], **Scott A. Hollingsworth**[1,2,3,4,9], **Franziska M. Heydenreich**[3,6], **Carl-Mikael Suomivuori**[1,2,3,4], **Connor Brinton**[1,2,3,4], **Raphael J.L. Townshend**[1,2,3,4], **Michel Bouvier**[6], **Brian K. Kobilka**[3], **Ron O. Dror**[1,2,3,4,5,11,*]

[1]Department of Computer Science, Stanford University, Stanford, CA 94305, USA

[2]Institute for Computational and Mathematical Engineering, Stanford University, Stanford, CA 94305, USA

[3]Department of Molecular and Cellular Physiology, Stanford University School of Medicine, Stanford, CA 94305, USA

[4]Department of Structural Biology, Stanford University School of Medicine, Stanford CA 94305, USA

[5]Biophysics Program, Stanford University, Stanford, CA, 94305, USA

[6]Department of Biochemistry, Institute for Research in Immunology and Cancer, Université de Montreal, Québec, Canada

[7]Present address: Department of Molecular and Cell Biology, University of California, Berkeley, Berkeley, CA 94703

[8]Present address: Department of Structural Biology, Genentech Inc., South San Francisco, CA 94080

[9]Present address: Department of Computational and Structural Chemistry, Merck & Co., South San Francisco, CA 94080

[10]These authors contributed equally

[11]Lead contact

Abstract

Binding of arrestin to phosphorylated G-protein-coupled receptors (GPCRs) controls many aspects of cell signaling. The number and arrangement of phosphates may vary substantially for a given

*Correspondence: matthieu.masureel@gmail.com (M.M.) or ron.dror@stanford.edu (R.D.).

Author contributions: N.L., M.M. and R.D. conceived the project. N.L., S.H., C-M.S., C.B, R.T., and R.D. designed, performed and analyzed simulations. M.M. purified and labeled arrestin constructs and designed and performed fluorescence spectroscopy experiments. N.L. and M.M. analyzed spectroscopic data. F.H. carried out in-cell experiments under supervision of M.B. N.L., M.M., B.K. and R.D. wrote the paper, with input from all authors.

Declaration of interests: B.K. is a cofounder of and consultant for ConfometRx, Inc.

GPCR, and different phosphorylation patterns trigger different arrestin-mediated effects. Here, we determine how GPCR phosphorylation influences arrestin behavior by using atomic-level simulations and site-directed spectroscopy to reveal the effects of phosphorylation patterns on arrestin binding and conformation. We find that patterns favoring binding differ from those favoring activation-associated conformational change. Both binding and conformation depend more on arrangement of phosphates than on their total number, with phosphorylation at different positions sometimes exerting opposite effects. Phosphorylation patterns selectively favor a wide variety of arrestin conformations, differently affecting arrestin sites implicated in scaffolding distinct signaling proteins. We also reveal molecular mechanisms of these phenomena. Our work reveals the structural basis for the longstanding 'barcode' hypothesis and has important implications for design of functionally selective GPCR-targeted drugs.

Graphical Abstract

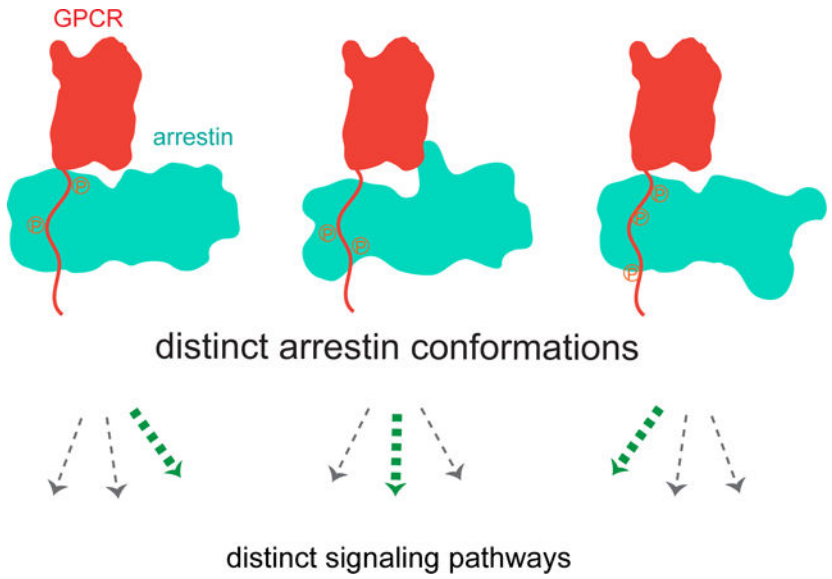

Introduction

Binding of arrestins to G-protein-coupled receptors (GPCRs), the targets of nearly half of all drugs, has myriad effects on cell signaling. Arrestins can desensitize GPCRs by blocking G-protein coupling. Arrestins can alter the effects of G-protein-mediated signaling by facilitating GPCR endocytosis. And arrestins can control a variety of intracellular signaling pathways by binding to an expansive set of effector proteins, including various kinases (e.g. ERK1/2, Akt, Raf-1, JNK, and Src), E3 ubiquitin ligases (e.g. Mdm2), deubiquitinating proteases (e.g. USP33), and Ca^{+2}–calmodulin (Gurevich and Gurevich, 2019; Peterson and Luttrell, 2017; Smith and Rajagopal, 2016; Tian et al., 2014).

Intriguingly, certain GPCR ligands selectively promote or suppress certain arrestin functions relative to both other arrestin functions and G protein signaling (Luttrell and Kenakin, 2011; Peterson and Luttrell, 2017). This has led to great interest in designing GPCR-targeted drugs that stimulate desired signaling effects without harmful side effects mediated by the same

GPCR, either by selecting between G protein and arrestin coupling or by selecting among arrestin-mediated signaling effects.

Evidence amassed over the past decade supports the ‘barcode’ hypothesis, which states that phosphorylation of different sets of GPCR residues leads to different arrestin-mediated signaling effects (Tobin, 2008). For example, preventing phosphorylation of certain residues impedes receptor endocytosis but not arrestin recruitment, whereas preventing phosphorylation of other residues impedes recruitment as well (Lee et al., 2016). GPCR ligands control arrestin phosphorylation patterns by modulating interactions of a GPCR with various G protein receptor kinases (GRKs), which phosphorylate different sets of GPCR residues (Busillo et al., 2010; Butcher et al., 2011; Inagaki et al., 2015; Komolov and Benovic, 2018; Nobles et al., 2011).

Despite strong evidence in favor of the barcode hypothesis, the molecular effects of different barcodes on arrestin, and the mechanism by which these effects arise, remain poorly understood. Biophysical studies have demonstrated that arrestins bound to differently phosphorylated GPCRs often adopt distinct conformations (Lee et al., 2016; Mayer et al., 2019; Nobles et al., 2011; Nuber et al., 2016; Yang et al., 2018; Yang et al., 2015). However, the actual conformations arrestin adopts—and the phosphorylation patterns leading to those conformations—remain largely unknown. Additionally, certain phosphorylation patterns modulate the affinity of a GPCR for arrestin, yielding signaling complexes with different stabilities (Bouzo-Lorenzo et al., 2016; Jung et al., 2017; Lee et al., 2016; Sente et al., 2018). However, whether phosphorylation-induced changes in arrestin conformation correspond to changes in arrestin binding remains unclear. Furthermore, to what extent do these effects depend upon the number of attached phosphates or upon which sites are phosphorylated?

To determine the molecular effects of phosphorylation barcodes on arrestin and the mechanism by which these barcodes encode arrestin behavior, we employed two complementary techniques—molecular dynamics (MD) simulations, which track the position of every atom, and site-directed spectroscopy, in which each spectrum reflects the local conformation of a specified arrestin region. We focus on the effects of a GPCR’s C-terminal tail (C-tail) on arrestin binding and conformation, because the C-tail contains many known phosphorylation sites that promote arrestin recruitment (Benovic et al., 1987; Lohse and Hoffmann, 2014). The C-tail can induce arrestin activation by binding either on its own or in concert with the GPCR’s transmembrane core (Cahill et al., 2017; Latorraca et al., 2018). For simplicity, most of our simulations and experiments examine the case where only the C-tail is present, but we demonstrate similar effects when the transmembrane core is also present.

We find that phosphorylation patterns affect both arrestin conformation and arrestin binding, but in very different ways. The effects depend primarily on the spatial arrangement of phosphorylated residues rather than the overall number of phosphates. We identify the molecular mechanism by which individual phosphates, and combinations of phosphates, alter arrestin behavior, and we explain how phosphates at various sites can have either stimulatory or inhibitory effects on arrestin binding and conformational change. We also find

that arrestin adopts a plethora of conformations, with different phosphorylation patterns favoring distinct conformations. Some phosphorylation patterns fail to expose sites that scaffold certain effector proteins, even though these patterns induce conformational changes elsewhere on arrestin, explaining how phosphorylation patterns can lead arrestins to stimulate certain downstream effects but not others. Our results not only show how GPCR-targeted drugs could selectively induce desired cellular effects by favoring specific phosphorylation patterns, but also provide a striking demonstration of how post-translational modification of a protein can provide a powerful control panel for the behavior of its binding partners.

Results

Arrestin binding and activation depend on spatial arrangement of phosphates

To determine how GPCR phosphorylation affects arrestin binding and conformation, we performed all-atom MD simulations of β-arrestin 1 bound to the V_2 vasopressin receptor (V_2R) C-tail, which contains eight phosphorylatable residues (Figure 1A) (Nobles et al., 2011; Shukla et al., 2013; Shukla et al., 2014). We performed simulations with all, none, and various subsets of these residues phosphorylated, including all 8 singly phosphorylated peptides and 20 peptides with two or three phosphorylated residues. We refer to each phosphopeptide as P_x, where x lists phosphorylated sites (e.g. P_2 denotes a peptide phosphorylated at the second site, Ser350). We use pX to denote phosphorylation of a specific site (e.g. p2 and pS350 both denote phosphorylation of Ser350). For each phosphopeptide–arrestin complex, we performed six independent simulations, each ~5.0 μs, totaling ~1 millisecond of simulation (Table S1).

In simulations of β-arrestin 1 bound to each phosphopeptide—including the fully phosphorylated and unphosphorylated peptides—arrestin fluctuated between inactive and active conformations, but the typical conformation differed widely depending on the specific phosphorylation pattern (Figures 1, S1). In the presence of the fully phosphorylated peptide, arrestin generally remained close to its crystallographic active conformation (Figure 1B). Upon removal of all phosphates from the V_2R C-tail—and in the absence of the V_2R C-tail altogether—arrestin typically relaxed to a conformation closely matching its crystallographic inactive conformation, with its C-terminal domain (C domain) twisting closer to the N domain (Figure 1B) (Latorraca et al., 2018). Partially phosphorylated peptides favored arrestin activation to widely varying degrees, with most favoring conformations intermediate between the crystallographic active and inactive conformations (Figure 1D). By activation, we refer to the global conformational change arrestin undergoes upon binding a fully phosphorylated GPCR, which is dominated by the interdomain twisting motion. We quantify extent of activation as described in Methods. Arrestin sometimes adopted a globally active conformation while certain localized regions retained their inactive conformations, and vice versa.

Phosphopeptides with the *same* number of phosphates favored arrestin activation to different degrees (Figure 1D, S1A). For example, one peptide with a single phosphate (P_2) favored active conformations nearly as much as the fully phosphorylated peptide, while another

singly phosphorylated peptide (P_3) favored the inactive conformation as much as the unphosphorylated peptide.

The various phosphopeptides also differed widely in their ability to bind arrestin tightly, as approximated by their stability in simulation (see Methods). Across peptides containing the same number of phosphorylated residues, some remained tightly bound while others exhibited markedly reduced stability. These observations indicate that overall ability of a phosphopeptide to bind β-arrestin 1 also depends on the specific positions of phosphorylated residues rather than on their total number (Figure 1D).

In some cases, adding a phosphate *reduced* arrestin activation or *weakened* binding. For example, adding a phosphate at S357 (p3) to the peptide with only S350 phosphorylated (compare $P_{2,3}$ vs. P_2) or only T360 phosphorylated (compare $P_{3,5}$ vs. P_5) significantly reduced activation (Figure 2B; $P = 0.04$ and $P = 0.05$, respectively; see Methods). Similarly, adding a phosphate at S362 (p6) to a peptide with only S350 phosphorylated (compare $P_{2,6}$ vs. P_2) significantly reduced binding stability (Figure 2E; $P = 0.01$).

Phosphorylation patterns favoring arrestin binding differ from those favoring arrestin activation

Interestingly, certain phosphorylation patterns favored binding more than they favored arrestin activation, while others favored activation more than binding (Figure 1D, S2C). For example, the peptide phosphorylated only at S363 (P_7) bound much more stably but did not significantly favor activation relative to the unphosphorylated peptide P_{none} (Figure 1D; $P = 3.2 \times 10^{-5}$ for binding; $P = 0.43$ for activation). $P_{2,3,4}$ favored activation more than other simulated peptides with three phosphates but bound less stably than many of these peptides. Thus, a GPCR C-tail with a particular phosphorylation pattern might potently recruit arrestin without triggering substantial activation-related conformational changes, while the same GPCR C-tail with a different phosphorylation pattern might induce conformational changes in arrestin despite binding to it only weakly.

To determine the average extent to which each phosphate contributes to binding and to activation, we fit additive regression models in which each residue makes an independent contribution to activation and to binding (Figure 2A,D). One phosphate, pT360 (p5), favored both activation and binding substantially. Phosphates pS350 (p2) and pT359 (p4) substantially favored activation with little contribution to binding, and pS363 (p7) substantially favored binding with little contribution to activation. Phosphorylation at S357 (p3) and S362 (p6) *inhibited* arrestin activation and binding, respectively.

Notably, the effect of phosphorylating a given residue often depends on which other residues are phosphorylated. For example, adding a phosphate at S362 (p6) to a peptide with only S350 phosphorylated disfavored arrestin activation (compare P_2 vs. $P_{2,6}$; $P = 0.029$), while adding the same phosphate to a peptide with both S350 and S363 phosphorylated favored arrestin activation (compare $P_{2,7}$ vs. $P_{2,6,7}$; $P = 0.015$).

To test whether the presence of the GPCR transmembrane core affects how phosphorylation patterns modulate arrestin behavior, we also simulated arrestin bound to a full-length GPCR.

We initiated these simulations from a recently solved structure of β-arrestin 1 in complex with the M_2 muscarinic acetylcholine receptor (M_2R) core ligated to the V_2R C-tail (Staus et al., 2020). We performed simulations with five C-tail phosphorylation patterns (Figure S3). We found that phosphorylation patterns have similar effects on arrestin activation in the presence and absence of the core, though presence of the core generally favors somewhat more active conformations. We also found that phosphorylation patterns typically have similar effects on arrestin binding with and without the core present.

How do distinct phosphorylation sites exert distinct effects?

Our simulations show that phosphates stimulate or inhibit global arrestin activation primarily by modulating the conformation of the gate loop, which extends off the arrestin C domain over the groove of the N domain to contact the bound GPCR C-tail. For example, pT359 (p4) and pT360 (p5) form a salt bridge with a lysine on the gate loop (K294), stabilizing the gate loop's active conformation; this mechanism matches the mechanism we previously observed for activation of visual arrestin by the phosphorylated rhodopsin C-tail (Latorraca et al., 2018). The active gate loop conformation keeps the C domain twisted away from the N domain, stabilizing a globally active conformation of arrestin. By contrast, pS357 (p3) inhibits arrestin activation by drawing K294—and thereby the entire gate loop—away from its active position (Figure 2B, C). While we focus here on the global interdomain twisting motion associated with activation, we show in the subsequent section that phosphates also modulate the conformation of local arrestin regions via other mechanisms.

Our simulations also show how phosphorylated residues that favor binding stabilize the GPCR C-tail's interactions with the arrestin N domain. The phosphates that most favor binding, such as pT360 (p5) and pS363 (p7), sit within pockets containing at least two positively charged residues, balancing the double negative charge contributed by the phosphate. These side-chain interactions 'lock' the phosphopeptide tail in place, stabilizing backbone-backbone hydrogen bonds formed between the β-stranded portion of the phosphopeptide and the arrestin N terminus. By contrast, pS362 (p6), which inhibits binding, does not pair with a cluster of basic residues to fully neutralize its charge in the crystallographic conformation. In simulation, p6 typically moved inward to interact with basic residues otherwise engaged by pT359 (p4) or pT360 (p5), and this motion often led the phosphopeptide to peel away from the arrestin N terminus, weakening phosphopeptide binding (Figure 2E, F). More generally, phosphates negatively modulate arrestin activation and/or binding when a particular phosphorylation pattern cannot properly balance electrostatic potential along the central groove of the arrestin N domain.

Arrestin populates a multi-dimensional space of conformations

In simulation, arrestin adopts a wide variety of conformations, and various arrestin regions —e.g., the finger loop, gate loop and interdomain crevice—each change conformation without requiring concomitant changes in other regions (Figure 3A, B). For example, the gate loop sometimes relaxed towards an inactive-like conformation even while the finger loop remained upright or the interdomain crevice remained open, close to their positions in the active, V_2R phosphopeptide–bound structure. When the gate loop adopted an active conformation, the interdomain crevice adopted an active conformation only 50% of the time

and the finger loop 60% of the time; when the finger loop adopted an active conformation, the gate loop adopted an active conformation only 40% of the time and the interdomain crevice 50% of the time. Local conformational changes of the finger loop and interdomain crevice are only loosely coupled to global arrestin activation (Figure 3B), as we previously observed for visual arrestin (Latorraca et al., 2018). Thus, arrestin populates a high-dimensional space of conformations rather than only conformations that interpolate between the inactive and active structures (Figure S4).

We also found that GPCR phosphorylation can affect the conformation of certain arrestin regions without affecting others (Figure 3C, S4). For example, phosphorylation at T360 (p5) strongly favored the active conformation of the gate loop, and in turn the global interdomain twisting motion associated with arrestin activation, but typically had little effect on the interdomain crevice or the finger loop. Phosphorylation at S350 (p2), on the other hand, strongly affected both the interdomain crevice and the finger loop but had little effect on the gate loop. Phosphate pS350 (p2) occupies the concave surface of the N domain, sterically preventing the finger loop from falling into that cavity. This phosphate also interacts with a basic residue on the middle loop, preventing this loop from falling into the interdomain crevice. Other phosphates may also predominantly affect specific regions of arrestin. For example, pT347 (p1) appeared to strongly favor active conformations of the finger loop in simulation, without substantially favoring active conformations of the remainder of the arrestin molecule. These results suggest that different phosphorylation patterns can select among a wide variety of arrestin conformations.

Site-directed spectroscopy to probe effects of phosphorylation patterns

We performed a number of experiments to test the key findings of our simulation study, namely that (1) arrestin activation and binding depend on the spatial arrangement of phosphates rather than on the number of phosphates; (2) phosphorylation patterns favoring activation often differ from those favoring binding; (3) arrestin populates a high-dimensional conformational space, with certain local regions changing conformation without requiring concerted changes in other regions; and (4) phosphorylation patterns can select among these many different arrestin conformations.

We chose a set of 14 phosphopeptides, all with the same V_2R C-tail sequence but with different phosphorylation patterns (Figure 4A). To monitor conformational effects of these phosphopeptides on arrestin, we used site-directed spectroscopy. We designed four β-arrestin 1 mutants, each with a chemical probe at a different site (Figure 4B). Three of these sites were chosen to detect local conformational changes at the gate loop, finger loop, and interdomain crevice, respectively. The fourth site, at the base of the arrestin C tail, was chosen to detect complete release of the arrestin tail from the arrestin body, as tail release enables the interdomain twisting associated with arrestin activation (Eichel et al., 2018; Latorraca et al., 2018). We quantified binding of each phosphopeptide to β-arrestin 1 by measuring displacement of a fluorescently labeled, fully phosphorylated peptide (Figure S5). These experiments are complementary to our simulations: the simulations capture atomic-level detail over microsecond timescales, whereas the experiments report on average

properties of conformational ensembles on the longer timescales associated with downstream signaling.

Certain phosphopeptides might bind arrestin in modes different from the phosphopeptide in the P_{all}–bound crystal structure, in which the arrestin C tail has been completely displaced by the bound phosphopeptide. We sought to select phosphopeptides that (1) displace the arrestin C tail and (2) typically bind in a register matching that observed in the structure (the starting point for our simulations). We thus required each experimental phosphopeptide to include phosphates pS363 (p7) and pS364 (p8). These phosphates facilitate binding in the crystallographic mode, in which they displace the arrestin C tail at its base. We refer to these peptides as P'_x, where x lists other phosphorylated sites. P'_{base} is phosphorylated only at S363 and S364, and P'_{all} is identical to and P_{all}.

We note that these experiments are not designed for, and do not enable, direct comparison between the behavior of a simulation with an individual phosphopeptide and an experiment with the same phosphopeptide. Due to the experimental objectives and the considerations described above, the simulations and experiments involve different sets of phosphopeptides. The simulations focus on the crystallographic binding mode, while some peptides appear to adopt additional binding modes experimentally (Table S2, Figure S5A, and discussion below). The experimental probes can only detect certain conformational changes in their surroundings, and the quantitative relationship between probe response and local conformation is unclear. Even without direct correspondence, however, the experimental results support each of the key findings of our simulation study.

At each of the four conformational reporters in our experiments, different peptides with the same number of phosphates have very different effects (Figure 4C). Depending on the phosphorylation sites, for example, addition of just two phosphates can cause no measured conformational change or approximately as much conformational change as the fully phosphorylated peptide.

Likewise, experimentally measured binding of arrestin to various phosphopeptides depends more strongly on phosphate positions than on number of phosphates, in agreement with predictions from simulation (Figure S5A, Table S2). Indeed, a ranking of phosphopeptides by either IC50 or maximal displacement of fluorescently labeled peptide (Emax) exhibits very low correlation with number of phosphates. Intriguingly, phosphorylation at site 6 (pS362) appeared to weaken binding, as in simulation: for example, all four peptides with this site phosphorylated have an experimentally determined binding affinity below the median (Figure S5A, Table S2).

As in simulation, effects of a given peptide on binding and conformation are often very different. Indeed, binding measurements hardly correlate with conformational change as detected by any of the four reporters. Peptides with similar log IC50 values in competition binding assays sometimes have very different conformational effects.

Our site-directed spectroscopy experiments also support other simulation-based findings (next two sections). These experimental results confirm that arrestin populates a high-

dimensional conformational space and that different phosphorylation patterns can select among many different conformations within that space (Figures 4C, 5A, 6A).

We performed additional experiments to verify that our findings persist in a cellular context and in the presence of the receptor transmembrane core. We generated several full-length V_2R constructs, each with mutations designed to eliminate all but a desired set of phosphorylation sites within the C tail (Figure S5C). We then measured agonist-dependent recruitment of β-arrestin 1 to the cell membrane by each V_2R construct, under conditions intended to favor phosphorylation of remaining sites on the receptor using enhanced bystander bioluminescence resonance energy transfer (ebBRET) (Namkung et al., 2016). These experiments come with caveats—most notably, the remaining phosphorylation sites might not be completely or uniformly phosphorylated for each mutant. Yet phosphorylation patterns appeared to have qualitatively similar effects to those we had observed previously. For example, including a phosphorylatable residue at site 7 instead of at site 6 led to increased arrestin recruitment, in agreement with our finding from biochemical experiments and simulations that p6 disfavors arrestin binding of phosphopeptides.

Phosphorylation patterns select among a wide variety of arrestin conformations

The most striking observations from our site-directed spectroscopy measurements (Figure 4C) are that different phosphorylation patterns favor different arrestin conformations and that the conformations of distinct arrestin regions do not change in concert as phosphorylation varies. That is, phosphorylation patterns select among a wide variety of arrestin conformations that do not fall along a continuum between the inactive and active structures, as demonstrated by principal components analysis of local conformational responses (Figure 5A, Table S3).

These observations support our computational findings that different arrestin regions can change conformation independently of one another and that GPCR phosphorylation can affect the conformation of certain arrestin regions without affecting others. The experimental results go beyond this, though, demonstrating that phosphorylation patterns can select among a strikingly wide variety of arrestin conformations and that these conformational differences persist even on the timescales associated with cellular signaling.

To further demonstrate that different arrestin regions can change conformation independently of one another, we repeated all site-directed spectroscopy measurements in the presence of an antibody fragment derived from Fab30 (Fab30*; see Methods), which stabilizes the active conformation of β-arrestin 1 (Shukla et al., 2013; Shukla et al., 2014). In this case, no phosphopeptide substantially affected the fluorescence of the reporter at the interdomain crevice, strongly suggesting that Fab30* locks this region of arrestin into a single conformational state (Figure 4C). Despite the presence of Fab30*, reporters at other regions of arrestin indicated that these regions changed conformation substantially in the presence of different phosphopeptides.

Our fluorescence spectroscopy results also indicate that local regions of arrestin, considered individually, adopt a wide variety of conformations as phosphorylation varies. This effect is particularly apparent for the finger loop, where spectra in the presence of different

phosphopeptides vary in both intensity and wavelength of peak emission (measures of solvent exposure and local polarity, respectively) (Kim et al., 2013) (Figure 5B). MD simulations also capture a wide variety of finger loop conformations differing markedly in the chemical environment of the fluorescent reporter (Figure 5C, S6).

Phosphopeptides can influence arrestin conformation without fully displacing the arrestin C tail

Interestingly, our site-directed spectroscopy results indicate that certain phosphopeptides trigger conformational change in arrestin without fully displacing the arrestin C tail (Figure 6A). For example, phosphopeptides P'_{base} and P'_2 had very little effect on the reporter at the base of the arrestin C tail but caused significant conformational changes in the gate loop. Simulations demonstrate how this behavior can arise. In simulations of full-length β-arrestin 1, with its entire C tail included, the upper portion of the arrestin C tail (*the distal tail*) fluctuates substantially in the upper groove of the N domain, while the lower portion (the *proximal* tail, which includes the reporter) remains tightly bound (Figure 6B). Nonetheless, removing the distal tail (residues 394–418) substantially increased the flexibility of the gate loop, finger loop, and C loop (Figure 6B, S6). A phosphopeptide could thus exert conformational effects on multiple regions of arrestin by displacing just the distal C tail and binding in its place—despite the fact that in available structures of active-state arrestins, the arrestin tail is fully displaced or removed.

Discussion

Our results reveal the molecular effects of GPCR phosphorylation barcodes on β-arrestin 1, as well as the mechanisms by which these effects arise, with key implications for arrestin function.

First, our findings imply that, by adjusting a GPCR's phosphorylation pattern, one can modulate some of arrestin's effects independently of others. For example, a GPCR could bind arrestin, thus blocking G-protein-mediated signaling, without triggering conformational changes required for arrestin-mediated signaling. A differently phosphorylated GPCR could alter arrestin conformation without forming a long-lived complex, leading to catalytic arrestin activation (Eichel et al., 2018).

Our results also imply that, by causing conformational changes only in certain regions of arrestin, a particular phosphorylation pattern could expose arrestin binding sites for some downstream signaling proteins but not others. For example, we find that certain phosphopeptides cause conformational change throughout arrestin without displacing the proximal tail. Full tail displacement is likely required for binding of certain downstream proteins to the proximal tail (e.g., adaptin) or to the arrestin N-terminal β-strand exposed by tail displacement (e.g., JNK3) (Park et al., 2019; Smith and Rajagopal, 2016; Tian et al., 2014). Biochemical and proteomic studies have suggested that β-arrestins interact with hundreds of proteins in the cell, with interaction sites on many arrestin surfaces (Coffa et al., 2011; Peterson and Luttrell, 2017; Tian et al., 2014; Xiao et al., 2007; Zhuo et al., 2020). Given the diverse effects of GPCR phosphorylation patterns on arrestin conformation, we expect that such patterns directly alter coupling of proteins with multiple regions of the

arrestin surface. In accord with this hypothesis, a recent NMR study suggested that differently phosphorylated peptides alter the conformation of arrestin regions thought to interact with kinase SH3 domains (Yang et al., 2018).

We find that the effects of phosphorylation depend much less on the number of residues phosphorylated than on their spatial arrangement. In certain cases, addition of a phosphate actually weakens arrestin binding or conformational effects on arrestin. One inhibitory phosphorylation site was previously reported on rhodopsin (Mayer et al., 2019). We find that multiple phosphorylation sites can have inhibitory effects, and that such effects may be specific to either arrestin binding or activation. Moreover, phosphorylation of a particular site may have either stimulatory or inhibitory effects depending on which other sites are already phosphorylated. Such inhibitory effects of phosphorylation could account for why a GPCR sometimes needs to *lose* phosphates to couple efficiently to arrestin or why the presence of multiple GRKs sometimes *reduces* arrestin signaling relative to that observed with a single GRK present (Butcher et al., 2011).

Based on analyses of crystal structures, Zhou et al. (2017) proposed a “phosphorylation code” for arrestin recruitment (i.e., binding). Our results are consistent with theirs but offer a much richer picture of the phosphorylation barcode. We find that the effects of a GPCR phosphorylation pattern on arrestin conformation—and thus on downstream signaling—are often very different from its effect on arrestin binding. We also find that a much wider variety of phosphorylation patterns can lead to strong arrestin binding than suggested by available structures, because the GPCR C-tail can change conformation such that other phosphates bind to the same pockets on arrestin. For example, pS350 (p2) often binds near the β-arrestin 1 pocket occupied by pS357 (p3) of V_2R in the crystal structure; indeed, pS350 generally contributes more favorably to arrestin binding than pS357, and pS357 actually tends to inhibit arrestin activation, whereas pS350 strongly favors activation.

Nearly all GPCRs couple either to β-arrestin 1 or to β-arrestin 2, which are highly similar in sequence and structure, particularly in the N domain where the GPCR C-tail binds. Even for GPCRs with C-tails very different from that of V_2R, control of arrestin behavior will most likely involve phosphate binding to some or all of the same sites on the arrestin surface, and phosphate binding at each of those sites will presumably have similar effects on arrestin binding and conformation. At certain GPCRs, phosphorylation of intracellular loops influences various arrestin functions (Butcher et al., 2011; Verweij et al., 2020; Yang et al., 2017); such phosphates may also interact at similar sites on arrestin (Huang et al., 2020). We find that the effects of GPCR C-tail phosphorylation patterns on arrestin are similar in the presence and absence of the GPCR’s transmembrane core (Fig. S3).

By revealing the varied effects of GPCR phosphorylation patterns on arrestin binding and arrestin conformation, our findings suggest unexplored opportunities for discovery of functionally selective drugs that stimulate desired signaling pathways without undesired ones at a given GPCR. Thus far, efforts to discover such drugs have focused on selecting for or against arrestin signaling relative to G-protein signaling—i.e., achieving arrestin bias or G-protein bias. Our results show how a drug that favors particular phosphorylation patterns of a GPCR could also select among arrestin’s many effects on cellular signaling, including

blockade of G-protein signaling, receptor internalization (leading to endosomal signaling), and direct stimulation of signaling proteins.

Our findings motivate further work: first, although previous studies have indicated a close relationship between arrestin conformation and signaling (Lee et al., 2016), the correspondence between specific arrestin conformations and specific signaling pathways remains unclear. How does arrestin's conformation affect its interactions with intracellular proteins, and how each interaction influence cellular signaling?

Second, further work is required to determine how ligands select among receptor phosphorylation patterns. Previous studies have demonstrated that, at many GPCRs, different ligands favor different phosphorylation patterns (Butcher et al., 2011; Mann et al., 2020; Mann et al., 2019; Miess et al., 2018; Nobles et al., 2011). For example, at the M3 muscarinic acetylcholine receptor, pilocarpine and metacholine induce phosphorylation at distinct sites (Butcher et al., 2011), and at the β_2 adrenergic receptor, carvedilol induces phosphorylation at two sites while isoproterenol induces phosphorylation at thirteen sites (Nobles et al., 2011). However, physiologically relevant phosphorylation patterns have not been catalogued exhaustively. Moreover, the receptor conformations that favor interaction with different GRKs—thus leading to different phosphorylation patterns—remain unknown.

Phosphorylation at protein–protein interfaces is a widespread phenomenon that plays an essential role in regulating diverse signaling pathways (Babu et al., 2012; Gulbis et al., 1996; Mittag et al., 2010; Nishi et al., 2013). Our results demonstrate the surprisingly rich set of conformational changes a protein can undergo in response to changes in the phosphorylation state of its binding partner, suggesting similar possibilities for many other protein families, including kinases and metabolic enzymes. We focused on GPCR–arrestin interactions because of their crucial role in drug action at the largest class of pharmaceutical targets (Hauser et al., 2017), but the approach taken here may illuminate such phenomena throughout the proteome.

STAR Methods

KEY RESOURCES TABLE

RESOURCE AVAILABILITY

Lead Contact

Further information and requests for resources and reagents should be directed to and will be fulfilled by the Lead Contact Ron Dror (ron.dror@stanford.edu).

Data and Code Availability

Molecular dynamics simulation data, including subsampled simulation trajectories, code, and metadata used to generate plots, can be found at http://dx.doi.org/10.5281/zenodo.3991060. Experimental datasets can be found in Mendeley Data at http://dx.doi.org/10.17632/nvwjmnsnjp.1.

Material Availability

Plasmids generated in this study will be distributed upon request. The BRET-based sensor used in the present study was licensed for commercial use to Domain Therapeutics but is available for academic research purposes upon request.

EXPERIMENTAL MODEL AND SUBJECT DETAILS

Bacterial strains

E. coli BL21(DE3) Rosetta cells were used to express ScdsFv30, and NiCo21(DE3) competent *E. coli* (NEB) were used to express all β-arrestin 1 constructs for *in vitro* spectroscopy studies.

Cell lines

For in-cell experiments, HEK293SL cells cultured in Dulbecco's modified Eagle's medium (DMEM) supplemented with penicillin/streptomycin and 10% newborn calf serum (NCS) were incubated for 48 h at 37 ºC with 5% CO_2.

METHOD DETAILS

System setup for molecular dynamics simulations

We simulated β-arrestin 1 on its own and bound to the V_2 vasopressin receptor (V_2R) C-tail (residues 346–368) with a variety of phosphorylation patterns, yielding more than 30 distinct simulation conditions in total. We initiated the majority of the simulations from the active-state crystal structure of β-arrestin 1 bound to the phosphorylated V_2R C-tail (PDB entry 4JQI) (Shukla et al., 2013). We simulated the following constructs: the active-state crystal structure with the fully phosphorylated peptide bound; the active-state crystal structure with the V_2R C-tail removed entirely; the active-state crystal structure with the V_2R C-tail bound but with all phosphorylated residues reverted to their phosphate-free serine or threonine identities; and the active-state crystal structure with different combinations of phosphorylated residues reverted to their phosphate-free serine or threonine identities. For simulations with phosphopeptides containing two or three phosphorylated residues, we excluded the two most peripheral phosphorylatable residues (Thr347 and Ser364), as they are located far from regions we previously identified as controlling global conformational changes in arrestin (Latorraca et al., 2018). See Figure 1 and Table S1 for a complete list of all simulation conditions.

We also performed simulations of β-arrestin 1 in its inactive state, in order to investigate (1) which conformations, besides the crystallographic conformation, different regions of arrestin adopted while in the inactive state (e.g. Figure 3B) and (2) how the arrestin C tail affected the global conformational ensemble of arrestin (e.g. Figure 6, Figure S4). We initiated simulations from two inactive-state crystal structures of β-arrestin 1 (PDB entries 1G4M and 1JSY) (Han et al., 2001; Milano et al., 2002). These two structures exhibit the same global conformation but differ slightly in that the arrestin C tail was truncated in the experimental 1G4M construct (and thus only residues 383–393 are resolved), whereas the full-length β-arrestin 1 was used to determine 1JSY (yielding six additional resolved tail residues, 394–

399). Simulations initiated from 1G4M and 1JSY exhibit similar behavior. We performed simulations of inactive-state β-arrestin 1 under the following conditions from the given PDB structure: with the crystallographic C tail resolved (PDB entry 1G4M); with the crystallographic C tail removed (PDB entries 1G4M and 1JSY); and with a full-length C tail modeled using the Rosetta FloppyTail application (Kleiger et al., 2009) (PDB entry 1JSY). We previously reported a subset of these simulations (Latorraca et al., 2018): simulations of active-state β-arrestin 1, with and without the V_2R C-tail, and simulations of inactive-state β-arrestin 1, with and without its crystallographic C tail (from the 1G4M structure).

For simulations starting from the active state of β-arrestin 1, we removed the co-crystallized Fab30 antibody. We used Maestro (Schrödinger) to revert phosphorylated residues to regular serines and threonines in order to generate different phosphorylation states of the V_2R C-tail. Simulations starting from the 1G4M inactive-state crystal structure used chain A. To model the full-length arrestin C tail, we first added unresolved residues 400–418 to the C tail of PDB entry 1JSY using PyMol and the human β-arrestin 1 sequence. We then used the FloppyTail application in Rosetta to generate approximately 50 different conformations and selected a conformation in which the C tail closely engaged residues on the N domain for subsequent simulations. We used the following general Rosetta parameters: use_input_sc; -packing:repack_only; run:min_type dfpmin_armijo_nonmonotone; and the following FloppyTail parameters: flexible_start_resnum 400; short_tail:short_tail_off 0; short_tail:short_tail_fraction 1.0; shear_on: 0.333; refine_repack_cycles 10; perturb_cycles 500; refine_cycles 100; and nstruct 50.

We performed multiple simulations for each condition, as specified in Table S1. For each simulation, initial atom velocities were assigned randomly and independently.

Simulation coordinates were prepared by removing non-protein molecules from all initial crystal structures (except for water molecules in structures 4JQI and 1G4M, which were retained during system preparation). Prime (Schrödinger) was used to model missing side chains and loops, as well as the fragment between residues 353 and 356 on the V_2R C-tail. We retained titratable residues in their dominant protonation state at pH 7. Histidines were represented with hydrogen on the epsilon nitrogen except in cases where addition of hydrogen to the delta nitrogen optimized the local hydrogen bond network.

All simulations were inserted into a water box using Dabble (Betz, 2017). Sodium and chloride ions were added to neutralize each system at a concentration of 150 mM. Water-box dimensions were chosen to maintain at least an 18 Å buffer between protein images in all dimensions. Initial system dimensions and number of atoms in each system are listed in Table S1 for each simulation condition.

We also initiated simulations of β-arrestin 1 bound to the transmembrane core of the M2 muscarinic acetylcholine receptor ligated to the V2R C-tail (M_2V_2R). For these simulations, we used the recent cryo-EM structure as a starting point (PDB entry 6U1N) after removing the Fab30 fragment (Staus et al., 2020). Due to the poorly resolved transmembrane region in that structure, we used the receptor from the M_2R–Go structure (PDB entry 6OIK), in which the receptor is well resolved, by aligning the receptor from the Go–bound structure onto that

of the β-arrestin-1–bound structure (Maeda et al., 2019). Missing side chains were modeled using Prime (Schrödinger) (Jacobson et al., 2002; Jacobson et al., 2004). The unresolved region of the C-tail (residues 458–486) was modeled using Modeller (Webb and Sali, 2014). The unresolved disordered region of ICL3 (~160 residues) was not modeled. Neutral acetyl and methylamide groups were added to cap the N- and C-termini, respectively, of the protein chains. Titratable residues were kept in their dominant protonation state at pH 7, except for D2.50 and D3.49, which were protonated, as evidence suggests that these residues are protonated for certain active-state class-A GPCRs (Ghanouni et al., 2000; Ranganathan et al., 2014). Histidines were represented with hydrogen on the epsilon nitrogen except in cases where addition of hydrogen to the delta nitrogen optimized the local hydrogen bond network. A palmitoyl group was added to residue C457 of the receptor using Maestro (Schrödinger). To simulate the different phosphorylation conditions, we reverted the relevant phosphothreonines and phosphoserines to threonines and serines, respectively, in Maestro. The systems were aligned on the receptor of the orientations of proteins in membranes (OPM) entry for the M_2R–Go structure (PDB entry 6OIK) (Lomize et al., 2012). Dowser was used to add water molecules to protein cavities (Zhang and Hermans, 1996), and the aligned structures were inserted into a pre-equilibrated palmitoyl-oleoyl-phosphatidylcholine membrane bilayer using Dabble (Betz, 2017). Sodium and chloride ions were added to neutralize each system at a concentration of 150 mM.

Simulation protocols

We performed our simulations using the Compute Unified Device Architecture (CUDA) version of Particle-Mesh Ewald Molecular Dynamics (PMEMD) in AMBER on one or two graphical processing units (GPUs) (Salomon-Ferrer et al., 2013). Simulations were performed using the AMBER16 and AMBER17 software (Case et al., 2017). Systems were heated from 0 K to 100 K in the NVT ensemble over 12.5 ps and then from 100 K to 310 K in the NPT ensemble at 1 bar over 125 ps, using 10.0 kcal mol^{-1} $Å^{-2}$ harmonic restraints applied to protein heavy atoms. Systems were then equilibrated at 310 K in the NPT ensemble at 1 bar, with harmonic restraints on protein heavy atoms tapered off by 1.0 kcal mol^{-1} $Å^{-2}$ starting at 5.0 kcal mol^{-1} $Å^{-2}$ in a stepwise fashion every 2 ns for 10 ns and then by 0.1 kcal mol^{-1} $Å^{-2}$ in a stepwise fashion every 2 ns for 18 ns. Production simulations were performed in the NPT ensemble at 310 K and 1 bar, using a Langevin thermostat for temperature coupling and a Monte Carlo barostat for pressure coupling. These simulations used a 4-fs time step with hydrogen mass repartitioning (Hopkins et al., 2015). Bond lengths to hydrogen atoms were constrained using SHAKE (Ryckaert et al., 1977). Non-bonded interactions were cut off at 9.0 Å, and long-range electrostatic interactions were computed using particle mesh Ewald (PME) with an Ewald coefficient of approximately 0.31 Å and a B-spline interpolation order of 4. The FFT grid size was chosen such that the width of a grid cell was approximately 1 Å. Trajectory snapshots were saved every 200 ps.

For simulations of the M_2V_2R, the simulation protocol was as described above, with the exception that harmonic restraints were placed on the non-hydrogen atoms of the lipids, protein and ligands during the heating phase. Similarly, during equilibration, harmonic restraints were applied to the non-hydrogen protein and ligand (but not lipid) atoms.

Simulations were performed with AMBER18, as they were performed more recently (Case et al., 2018).

For all simulations, we used the CHARMM36 force field for proteins, lipids, and ions and the TIP3P model for waters (Best et al., 2012; Huang and MacKerell, 2013; Klauda et al., 2010; MacKerell et al., 1998). Parameters for the orthosteric M_2R agonist iperoxo and the positive allosteric modulator LY2119620 were based on the CHARMM General Force Field (CGenFF) webserver (https://cgenff.umaryland.edu/; Vanommeslaeghe et al., 2010; Vanommeslaeghe and MacKerell, 2012; Vanommeslaeghe et al., 2012). Parameters are available upon request.

Analysis protocols for molecular dynamics simulations

The AmberTools17 CPPTRAJ package was used to reimage and center trajectories, while Visual Molecular Dynamics (VMD) was used to visualize and analyze simulations (Humphrey et al., 1996; Roe and Cheatham, 2013b). Time traces from simulation were smoothed using a rectangular moving average with a window size of 50 ns and visualized with the PyPlot package from Matplotlib.

For all analysis in the manuscript that required structural alignment, we aligned β-arrestin-1 structures on the N domain of β-arrestin 1 (to residues 6–173 of the N domain of either the active-state or inactive-state β-arrestin-1 structure, unless otherwise specified).

To characterize global β-arrestin-1 conformation, we employed two metrics described previously (Latorraca et al., 2018): a projection metric and an interdomain twist angle. The first, referred to as the “activation” metric in Figure 1, specifies how ‘active-like’ or ‘inactive-like’ a conformation is. We represent the positions of all atoms of interest for simulation frames (in this case, all Cα atoms except for residues 331–340, which are not resolved in the inactive-state crystal structures, PDB entries 1JSY and 1G4M) as a single vector containing their Cartesian coordinates. We project the vector representing the region of interest in a given simulation frame onto the line connecting the crystallographic inactive (from PDB 1JSY) and active conformations (PDB entry 4ZWJ) after aligning on Cα atoms in the N domain. We then report the position of the projected point on the line, using the convention that the inactive conformation is at 0 and positive values indicate change towards the active conformation. The crystallographic active conformation is thus assigned a value equal to its r.m.s.d. from the inactive conformation. We also calculated an interdomain twist angle, which corresponds to how much the C domain twists away from its position in the inactive crystal structure relative to the N domain. Briefly, we measured rotation about the rotation axis that defines displacement of the C domain (relative to the N domain) between the inactive β-arrestin 1 crystal structure (PDB entry 1G4M) and the active, rhodopsin-bound visual arrestin crystal structure (PDB entry 4ZWJ). (For both the rotation and projection metrics, we use the full-length receptor-bound structure as it captures the conformational change upon activation better than the active β-arrestin 1 crystal structure, whose interdomain twisting is slightly influenced by the presence of co-crystallized Fab30.) Thus, the inactive-state structure has an interdomain twist angle of 0º, positive interdomain twist angles indicate motion towards the active conformation, and negative interdomain twist angles indicate motion in the opposite direction. The projection metric and interdomain twist

angle are highly correlated (Figure S1), but in this manuscript we primarily use the projection-based metric to describe activation, because it takes into account the global conformation of arrestin, including rearrangements in loops, and therefore avoids the assumption that the *only* change associated with activation is rotation of the two lobes about a single axis. We also use local measures of conformational change in arrestin (as shown in Figure 3) as well as crystal structure–agnostic metrics (Figure S4) to further characterize arrestin's conformational ensemble.

For box plots, distributions for each simulation condition are based on samples taken every 1 ns across *all six simulations* for each condition, after removing the first 1000 ns of each simulation to allow for system equilibration. Interquartile ranges, shown as boxes, depict the 25^{th} and 75^{th} percentiles of each of these distributions, which are composed of tens of thousands of simulation frames. When shown, whiskers represent the 5^{th} and 95^{th} percentiles of the distributions for each simulation condition. Note that in certain supplementary figures, we overlay box plots, representing the entire distribution for an individual phosphorylation pattern after removing the first 1000 ns, and individual points, representing the mean values for each of the independent simulations within a given condition.

To calculate whether differences among pairs of conditions are statistically significant, we performed a two-sided Welch's *t*-test (two-sided *t*-test of unequal variance), treating each independent simulation's mean as a separate data point. We performed six production simulations under each condition ($n = 6$), excluding the first 1000 ns of each simulation to achieve better equilibration. For these analyses, we excluded simulation 3 of the P_3 condition, because in this simulation, the N domain distorts significantly from the conformations observed in the inactive-state and active-state crystal structures. This simulation is included in our deposited dataset.

To calculate strength of binding of each V_2R C-tail phosphopeptide in simulation, we quantified the stability of the phosphopeptide by calculating the root-mean-square deviation (r.m.s.d.) of Cα atoms from residues 360–365 of the V_2R C-tail relative to their crystallographic position in the structure of β-arrestin 1 in complex with the fully phosphorylated V_2R C-tail after aligning on the N domain. We report stability as 6 Å – r.m.s.d, such that lower values correspond to weaker binding and higher values correspond to stronger binding; the value 6 Å is chosen such that this difference remains positive.

We focused primarily on stability of the distal portion of the GPCR C-tail (C-terminal residues 360–365 of V_2R), as these residues form backbone-mediated hydrogen bonds with arrestin in the phosphopeptide-bound β-arrestin 1 crystal structure (Shukla et al., 2013). We also note that the phosphopeptide must compete with the arrestin C tail (residues 385–390) to bind to the same site on arrestin. Thus, it stands to reason that phosphopeptides that bind tightly to the body of arrestin would also favor arrestin C-tail displacement. In Figure S2A, we also count the number of backbone–backbone hydrogen bonds between residues 360–365 of the phosphopeptide and residues 6–10 of the arrestin N terminus that persist over the course of the simulation. This measure of backbone-mediated hydrogen bonding correlates well with GPCR C-tail stability.

To estimate the typical contribution of phosphorylation at each site to extents of activation and binding, as shown in Figure 2, we performed linear regression on the median activation and binding values for each simulation.

To characterize the conformation of local regions in β-arrestin 1, shown in Figure 3, we used several different metrics. To characterize motion at the base of the gate loop, we measured the projection of the position of the Cα atom of D290 in simulation onto the vector separating the inactive and active crystallographic positions of the same atom. Higher values (close to 1.6 Å) indicate that the gate loop has shifted away from the body of the N domain, a motion associated with favoring the active conformation, while lower values (close to or less than 0.0 Å) indicate that the gate loop has shifted toward the body of the N domain, a motion associated with favoring the inactive conformation. For this metric, we used the visual arrestin crystal structures as references (PDB entries 1CF1, chain A, and 4JQI) to enable comparisons with our previous work (Hirsch et al., 1999; Latorraca et al., 2018; Shukla et al., 2013). To characterize the conformation at the 'tip' of the gate loop, we measured the projection of the positions of the Nζ atom of K294 onto the stationary vector defined by the Cα atoms of R7 and R165 in the active-state β-arrestin 1 crystal structure (PDB entry 4JQI). For the Nζ atom of K294, values close to 11.9 Å, respectively, indicate that the gate loop is in a conformation close to that favored by the fully phosphorylated peptide. We subtract the raw position of the atom along the vector from its initial position (11.9 Å), take the absolute value of this, and negate it, such that values of 0 represent values close to the crystallographic active conformation of the gate loop, and increasingly negative numbers represent values far from the active conformation of the gate loop. To quantify finger loop conformation, we project the position of the simulated position of L68 onto the vector defined by the inactive (PDB entry 1JSY) and active crystallographic positions of the same atom. To quantify interdomain crevice opening, we calculate the distance between the center of mass of a pair of Cα atoms on the middle loop (residues 131 and 139) and a pair of Cα atoms on the C loop (residues 247 and 249). To generate the plots in Figure 3C and Figure S4B, we aggregated data across all simulations after removing the first 1000 ns of each to ensure system equilibration.

To classify the conformation of these different local regions, as in Figure 3B, we set thresholds based on conformations observed in simulations of active-state β-arrestin 1 bound to the fully phosphorylated peptide ("active control simulations") and inactive-state β-arrestin 1 ("inactive control simulations"). For the gate loop, we used motion at its base (D290) instead of at its tip (K294), as the arrestin C tail constrains the tip of the gate loop to one particular inactive conformation in the inactive-state β-arrestin 1 simulations. Using the metrics described in the previous paragraph, regions were classified as adopting an active conformation if they adopted conformations within half the standard deviation of the active control simulations (global activation: ≥ 3.0 Å º; gate loop: ≥ 1.45 Å; finger loop: ≥ 16.2 Å; interdomain crevice: ≥ 13.5 Å), after removing the first 1500 ns of simulation to ensure system equilibration. Regions were classified as adopting an inactive conformation if they adopted conformations within half the standard deviation of the inactive control simulations (global activation: ≤ 0.8 Å; gate loop: ≤ 0.31 Å; finger loop: ≤ 6.22 Å; interdomain crevice: ≤ 10.9 Å). In the text, we report fractions of the time that simulations populate a given state only for simulations starting from the active conformation of arrestin. To generate plots in

Figure 3B, we first smoothed the conformational values for each metric using a sliding average with a window of 50 ns. Plots in Figure 3B are truncated at 4.5 μs as the corresponding simulations differ slightly in length (Table S1).

To map the conformational landscape of β-arrestin 1 in the presence of different phosphopeptides, we performed time-lagged independent component analysis (tICA) using MSMBuilder2 (Beauchamp et al., 2011) on structural features representing three regions of β-arrestin 1: inter-residue contacts for the interdomain crevice, involving residues on the middle loop and C loop; dihedral angles for atoms in the finger loop; and dihedral angles for the gate loop, using simulation trajectories downsampled to one frame every 10 ns (for computational efficiency). To featurize the interdomain crevice, we used the ContactFeaturizer using the *closest-heavy* scheme on residues in the middle loop (127, 129, 132, 140, 142), the C loop (239, 241, 243–246, 248, 249, 251), a portion of the lariat loop (286–288) and the back loop (313, 314, 316, 317 and 319). To featurize the finger loop, we used the DihedralFeaturizer on residues 60–80 with sine and cosine values for the phi, psi, omega, chi1, chi2, chi3, and chi4 angles. We performed dimensionality reduction using tICA with a lag time of 10 ns and 10 components on scaled feature vectors. To generate cluster centers roughly corresponding to distinct macrostates, we performed mini-batch K means clustering with 50 clusters, constructed a Markov State Model (MSM) with a lag time of 50 ns, and then performed kinetic lumping with PCCAPlus to identify the 8 clusters whose centers are shown as circles in Figure S4. As our intention was simply to provide a description of the spread of conformations in our simulation, and not to generate a rigorously Markovian model, we did not extensively vary model parameters. However, our key observations—including that arrestin populates a high-dimensional space of conformations—hold across different combinations of tICA lag times, numbers of clusters, MSM lag times, and numbers of macrostates.

For Figure 5C, which shows snapshots of the arrestin finger loop, simulation frames shown are from simulation 5 of the $P_{3,4,5}$ condition, except for the upper-left image, which was taken from simulation 1 of arrestin in its inactive state with its full-length C tail modeled.

Protein constructs & plasmids

The full-length long splice variant of human, cysteine-free (C59V, C125S, C140L, C150V, C242V, C251V, C269S) β-arrestin 1 was modified with an N-terminal 6x histidine tag, followed by a 3C protease site, a GG linker, AviTag and GGSGGS linker. The sequence was codon-optimized for expression in *E. coli* and cloned into a pET-15b vector. Individual constructs were made in this background by introducing the following mutations, respectively: L68C, N245C, V167W-L293C, V387C. Several previous studies have successfully attached site-specific probes at these and nearby sites to monitor local arrestin behavior (Kim et al., 2013; Peterhans et al., 2016; Sommer et al., 2012; Zhuo et al., 2014). The disulfide-stabilized single-chain Fv fragment of Fab30 (scdsFv30, which we also refer to as Fab30*) was derived from Fab30 by joining the variable regions of the light chain (V_L) and heavy chain (V_H) with a flexible linker (GTTAASGSSGGSSSGA) and inserting an interchain disulfide bond between V_H44 and V_L100 (Kabat numbering).

Protein expression, purification and labeling

ScdsFv30 was expressed in *E. coli* BL21(DE3) Rosetta cells as an N-terminal MBP fusion followed by a 3C protease tag and purified by nickel affinity chromatography through a C-terminal 8x histidine tag, as previously described (Shukla et al., 2013; Shukla et al., 2014). Final purification was performed by size-exclusion chromatography (GE Superdex 200) in 20 mM Hepes, pH7.4, 100 mM NaCl. The purified protein was then concentrated using a 50 kDa spin concentrator and aliquots were flash-frozen in liquid nitrogen and stored at −80 °C until use.

All β-arrestin 1 constructs used were prepared as follows: NiCo21(DE3) competent *E. coli* (NEB) were transformed, and large-scale cultures were grown in TB + ampicillin at 37°C to an OD_{600} of 1.0. Cells were then transferred to room temperature and induced with 25 μM IPTG when the OD_{600} reached 2.0. Cells were harvested 20 h post induction and resuspended in lysis buffer (50 mM Hepes pH 7.4, 500 mM NaCl, 15% glycerol, 7.13 mM BME) to a final volume of 40 mL/L of cells. Cells were lysed by sonication, and the clarified lysate was applied to nickel sepharose and batch incubated for 1.5 h at 4 °C. The resin was washed with ten column volumes of wash buffer (20 mM HEPES pH 7.4, 500 mM NaCl, 10% glycerol, 7.13 mM BME) + 20 mM imidazole, followed by ten column volumes of wash buffer + 40 mM imidazole. The protein was then eluted with five column volumes of wash buffer + 200mM imidazole and dialyzed overnight in 100x volume of dialysis buffer (20 mM Hepes 7.4, 200 mM NaCl, 2 mM BME, 10% glycerol) in the presence 3C protease, with a protease:arrestin ratio of 1:10 (w:w). The digested protein was then subjected to reverse-nickel purification and diluted with dialysis buffer containing no NaCl to bring the NaCl concentration to 75 mM. The protein was then purified by ion-exchange chromatography (mono Q 10/100 GL, GE Healthcare) by running a salt gradient from 75 mM to 400 mM in 20 mM Hepes pH 7.4, 2 mM BME, 10% glycerol. The elution peak fractions were then pooled, concentrated using a 30 kDa spin concentrator and subjected to size-exclusion chromatography using a Superdex 200 increase 10/300 GL column (GE Healthcare) in SEC buffer (20 mM HEPES pH 7.4, 300 mM NaCl, 10% glycerol). Following this, elution peak fractions were pooled to a concentration of 10–20 μM and labeled with either spin label or fluorophore: mBBr, Thermo Fisher Scientific M1378; IANBD, Thermo Fisher Scientific D2004; or S-(1-oxyl-2,2,5,5-tetramethyl-2,5-dihydro-1H-pyrrol-3-yl)methyl methanesulfonothioate (MTSSL), Enzo Life Sciences ALX-430–134. Spin label or fluorophore was dissolved at 10 mM in DMSO and added at a 10x molar excess over protein and allowed to react for 1 h at room temperature. The sample was then subjected to a second round of size-exclusion chromatography, as detailed above, to remove free dye. The purified, labeled protein was then concentrated to 200–300 μM using a 30 kDa spin concentrator, and aliquots were flash-frozen in liquid nitrogen and stored at −80 °C until use. β-arrestin 1 construct L68C was labeled with monobromobimane (L68BIM); constructs N245C and V167W/L293C were labeled with IANBD (N245NBD and V167W/L293NBD, respectively); and construct V387C was labeled with MTSSL (V387R1).

Peptides

Peptides were obtained by custom peptide synthesis (Tufts University Core Facility). The purified peptides were weighed and dissolved in 100mM Hepes pH 7.4 to a concentration of

~5mM. Exact concentrations of unlabeled peptides were then determined by Ellman's assay, where DTNB reacts with the sulfhydryl group of the individual cysteine present in each peptide to yield a colored product that is readily quantified by spectrophotometric measurement. To do so, DTNB (Thermo Fisher Scientific 22582) was dissolved in reaction buffer (20mM Hepes pH 7.4, 100mM NaCl, 1mM EDTA) at a concentration of 200 μM and mixed in a 9:1 (v:v) ratio with a 10x dilution of each peptide stock. Samples were then incubated in the dark for 30 minutes and the absorbance at 412 nm was measured in a clear-bottom 96-well plate on a SpectraMax Paradigm plate reader (Molecular Devices). A similar procedure was followed using a dilution series of cysteine to generate a reference standard curve from 0–1500 μM cysteine, from which peptide stock concentrations could then be calculated. All measurements were performed in triplicate.

FITC-labeled, fully phosphorylated V_2R C-tail peptide was dissolved to a stock concentration of ~1mM in 100 mM Hepes pH 7.4, after which the exact concentration was determined by diluting the stock appropriately to be in a linear absorbance range and by measuring the FITC absorbance at 495 nm. Using the chosen dilution factor and the reported extinction coefficient at pH 7.5 of 84000 cm^{-1} M^{-1}, the exact stock concentration was calculated.

Fluorescence polarization spectroscopy

Measurements were performed and analyzed based on guidelines described previously (Moerke, 2009; Rossi and Taylor, 2011). The FITC-labeled peptide was used at a final concentration of 4 nM in all assays. For saturation binding experiments, a two-fold dilution series in 20 mM Hepes pH 7.4, 100 mM NaCl, 0.01 % (w/v) DDM of unlabeled cysteine-free β-arrestin 1 was made from a 50 μM stock of β-arrestin 1, yielding twelve samples with final concentrations ranging from 47.8 μM to 0.02 μM. Each of these samples was incubated with FITC-labeled peptide for 1 h at room temperature prior to measurements, and for each peptide dataset, a control sample containing no β-arrestin 1 was included to measure the free anisotropy of FITC-labeled peptide. For competition binding experiments, β-arrestin 1 was used at a final concentration of 2.5 μM. A twofold dilution series of each unlabeled competing peptide was then prepared, yielding a concentration range from ~1 mM to ~1 nM, with exact values calculated for each peptide series based on the determined stock concentrations. Samples were incubated for 1h at room temperature prior to measurements. Saturation binding measurements of FITC-P'_{all} were performed in triplicate and competition binding experiments in quadruplicate in a 384-well plate on a Tecan Infinite M1000 (Tecan Life Sciences), using an excitation wavelength of 470 nm, an emission wavelength of 525 nm and excitation and emission bandwidths of 5 nm. The obtained data was fit using "One Site – Total" (for saturation binding) and "One Site – Fit logIC50" (for competition binding) nonlinear regression methods with Graphpad Prism 8. Specificity of binding in the assay was validated by obtaining the same FITC-P'_{all} / P'_{all} affinity values from saturation and competition binding experiments (0.73 uM, 0.37 uM respectively). Error bars reported in Figure S5 represent the standard error of the fit for each peptide.

Fluorescence emission spectroscopy

Bimane-labeled and NBD-labeled β-arrestin-1 constructs were used at final concentrations of 0.2 μM in buffer containing 20 mM HEPES pH 7.4 and 100 mM NaCl. Peptide stocks were used at a final concentration of 175 μM, a concentration chosen to achieve at least 90% occupancy of β-arrestin 1 based on the measured affinities that range from ~1 μM to ~20 μM. To avoid any nonspecific vehicle effects, care was taken to add the same total amount of peptide stock buffer (100 mM Hepes pH 7.4) in all samples. Samples were incubated at the final concentrations used for 1 h in the dark before measurements. Fluorescence data were collected in a quartz cuvette with 130 μL of sample using FluorEssence v3.8 software on a Fluorolog instrument (Horiba) in photon-counting mode. Bimane fluorescence was measured by excitation at 370 nm with excitation and emission bandwidth passes of 4 nm, and emission spectra were recorded from 430 to 500 nm in 1 nm increments with 0.5 s integration time. NBD fluorescence was measured by excitation at 490 nm with excitation and emission bandwidth passes of 5 nm, and emission spectra were recorded from 520 to 590 nm in 1 nm increments with 0.5 s integration time. Measurements were performed in triplicate, with each spectrum averaged from two scans, and care was taken to extensively rinse and air-dry the cuvette between each individual measurement. To remove background fluorescence, buffer spectra were collected using the same settings, and subtracted from each sample spectrum.

We calculated the relative response values shown in Figure 4C as follows. For each individual spectrum, we determined the maximum emission intensity (termed iMax). As noted above, we measured three spectra for each β-arrestin-1 reporter construct under each condition; we averaged the iMax values for these three spectra to obtain an average iMax value. We then normalized (scaled) all iMax values such that the maximal normalized average iMax value for each β-arrestin 1 reporter construct was 100, with all other iMax values for the same β-arrestin 1 reporter construct scaled accordingly. Following β-arrestin 1 activation upon addition of peptides, most iMax values for reporter constructs L68BIM and N245NBD increase. For reporter construct L293NBD/V167W, however, most iMax values decrease upon activation, due to increased quenching of the fluorophore by V167W. To facilitate visualization and interpretation of the data, L293NBD/V167W iMax values were inverted to also show an increase upon activation. This was done by transforming normalized iMax values to iMax* values as follows: $iMax^*=[(iMax_{Min}+iMax_{Max})–iMax]$, where $iMax_{Min}$ and $iMax_{Max}$ are the smallest and largest normalized average iMax values for this reporter construct, respectively. Individual dots in Figure 4C correspond to normalized iMax values for L68BIM and N245NBD, and to iMax* values for L293NBD/V167W. Bars in Figure 4C correspond to normalized average iMax values for L68BIM and N245NBD, and to average iMax* values for L293NBD/V167W. Error bars represent standard deviation of three replicates.

Electron paramagnetic resonance (EPR) spectroscopy

To ensure sufficient signal sensitivity, reporter construct V387R1 was used at a final concentration of 25 μM, and peptides were added to a final concentration of 175 μM. Measurements were performed on a Miniscope MS400 (MagnetTech) operating at X-band (9.43 GHz). Samples (50 μL) were placed in calibrated glass capillaries and spectra were

recorded at 22 °C over 11.9119 mT with an incident microwave power of 10 mW, a modulation frequency of 100 kHz, and a modulation amplitude of 0.050 mT. All EPR spectra, plotted as the first derivative of the absorbance, were baseline corrected and each spectrum was normalized relative to its total spin label concentration. Measurements were performed in triplicate, with each spectrum averaged from two scans. The left-field peak intensity maximum (iMax) was then determined from each spectrum. iMax values were averaged and normalized as described above for fluorescence spectra. Individual dots in Figure 4C correspond to normalized iMax values, and bars correspond to normalized average iMax values.

To understand better how the conformational response of β-arrestin 1 to individual peptides varied, we performed principal components analysis (PCA) to convert the eight average responses (four conformational readouts, each performed with and without Fab30*) of each of the 14 peptides into a lower dimensional space. Before PCA, data were scaled such that each response had the same variance across peptides. The first several principal components accounted for the following percentages of the variance in the data: PC1 = 60%, PC2 = 20%, PC3 = 12%, and PC4 = 4%.

In-cell experiments

BRET-based biosensor plasmids coding for luciferase-tagged β-arrestin and the membrane-anchored rGFP-CAAX have been previously described (Namkung et al., 2016). The sequences coding for SNAP-tagged vasopressin V_2 receptor (V_2R) variants were partially synthesized and subcloned by GenScript (Piscataway, NY, USA).

Human embryonic kidney cells (HEK) 293 SL cells were cultured in Dulbecco's modified Eagle's medium (DMEM, Wisent Bio Products, CA) supplemented with penicillin/streptomycin (Wisent Bio Products) and 10% newborn calf serum (NCS). The HEK293SL cells were transiently transfected with biosensor and V_2R variant DNA using linear 25-kDa polyethyleneimine (PEI, Polysciences, Warrington, PA, USA) diluted to 0.03 mg/ml using 100 µl biosensor plasmid dilution plus 100 µl PEI dilution. The cells were then seeded into white Cellstar® PS 96-well plates (Greiner Bio-One, Germany) at a density of 20,000 cells per well. After 48 h incubation at 37°C with 5% CO_2, the cells were washed with Tyrode's buffer (NaCl 137mM, KCl 0.9mM, $MgCl_2$ 1mM, $NaHCO_3$ 11.9mM, NaH_2PO_4 3.6mM, Hepes 25mM, glucose 5.5mM, $CaCl_2$ 1mM pH7.4). 90 µl of Tyrode's buffer were added to each well and the plates were stored at 37°C with 5% CO_2 for at least 30 min before the measurement. The cells were incubated with 10 µl 10x ligand stock (arginine-vasopressin in PBS for 5 min and then 10 µl coelenterazine 400a (DeepBlueC, NanoLight Technology, Pinetop AZ, USA) at a final concentration of 2.5 µM for another 5 min. The fluorescence was measured at 400 and 510 nm in a Synergy Neo plate reader (Biotek, Canada) using a dual PMT filter cube (part number 1035072). Each experiment was carried out in biological triplicates with internal quadruplicates.

Receptor expression levels were tested by cell-surface ELISA using an anti-SNAP antibody. 96-well cell culture plates were coated with poly-D-lysine to improve cell adherence. Transfected cells were seeded at 20,000 cells per well and incubated at 37°C for 48 h. The cells were then washed with PBS and fixed with 3% paraformaldehyde for 10 min. The cells

were washed three times with PBS + 0.5% BSA, for the last wash steps, the buffer was left in the wells for 10 min before removal. 50 µl of primary rabbit anti-SNAP antibody (GenScript) at 0.25 µg/ml were added to the cells and incubated for 1h at RT. The wells were washed as described before. 50 µl of 1:1000 diluted secondary anti-rabbit HRP antibody (GE Healthcare) were added. After a 1 h incubation step at room temperature, the cells were washed three times with PBS+0.5% followed by three washes with PBS. Wash steps were performed as described before. Per well, 100 µl SigmaFast OPD solution (Sigma Aldrich) were added, the plates were protected from light and incubated at RT. The reactions were stopped by addition of 25 µl 3M HCl. 100 µl of the solution were transferred to a transparent 96-well plate and the OD was read at 492 nm using a Tecan GENios Plus microplate reader. Each experiment was carried out in internal quadruplicates on two separate transfections. All data were analyzed in GraphPad Prism 7 (GraphPad, San Diego Ca, USA).

QUANTIFICATION AND STATISTICAL ANALYSIS

To determine whether a pair of simulation conditions (e.g., simulations with two distinct phosphorylation patterns) exhibited significantly different behavior in terms of arrestin activation and binding, we employed a two-sided *t*-test of unequal variance (Welch's *t*-test). We treated each independent simulation's mean as a separate data point. Each condition typically had six simulations ($n = 6$); see Table S1 for a list of all simulation conditions. Statistical comparisons relating to these data appear in the text and are related to Figure 1, Figure S1 and Figure S3.

Throughout the manuscript, we report box plots to characterize the spread of activation and binding values observed for a given simulation condition. To construct box plots, we use values sampled every 1 ns from every simulation within a condition, after removing the first 1000 ns of each simulation. Box plots thus represent an aggregate over all simulations in a condition. Each box extends from the 25^{th} percentile to the 75^{th} percentile, with a white vertical line indicating the 50^{th} percentile (the median). Box plots appear in Figure 1, Figure 2, Figure S1 and Figure S3. Please see the Method Details, as well as the captions of Figure 1, Figure 2, Figure S1, and Figure S3, for further specifics regarding choice of metrics used to describe changes observed in simulation.

Bar plots for spectroscopy data shown in Figure 4 and Figure 6 represent mean values for each measurement carried out in triplicate; error bars represent the standard deviation over the three measurements. In Figure 6, two-sided *t*-tests of unequal variance were performed to compare one condition to another; a significance cutoff of P=0.05 was used to determine whether a difference was significant. For fluorescence polarization experiments, shown in Figure S5B, the data was fit using the "One Site – Fit logIC50" (for competition binding) and "One Site – Total" (for saturation binding; only applicable to the P'_{all} peptide) nonlinear regression methods with Graphpad Prism 8. Error bars in Figure S5A show the standard deviation of reported values across three replicates for the P'_{all} peptide. Figure S5B shows the standard error of the fit for competition binding for each peptide.

For β-arrestin 1 recruitment assays (Figure S5C), error bars represent the standard deviation across three replicates. For ELISA measurements, error bars represented pooled standard deviations across two replicates (four statistical replicates each).

In Figure 5A, we report the results of principal components analysis on the data shown in Table S3. We report variation along the first two principal components, which account for 60% and 20% of the variance in the dataset, respectively.

The *t*-tests described above assume that datapoints under each condition come from a normal distribution. The individual datapoints (Figure S1, Figure S3, Figure 6) appear consistent with this assumption, but given the small number of data points under each condition, we did not perform quantitative tests of this assumption.

Supplementary Material

Refer to Web version on PubMed Central for supplementary material.

Acknowledgments:

We thank R. Betz, J. Paggi, A.J. Venkatakrishnan, A. Koehl, K. Larsen, M. Sommer, D. Veprintsev and D. Mayer for assistance and discussion. Funding: National Institutes of Health grants R01GM127359 (R.D.) and R01NS028471 (B.K.) and Canadian Institute of Health Research grant FDN#148431 (M.B.). This research used resources of the Oak Ridge Leadership Computing Facility, a DOE Office of Science User Facility supported under Contract DE-AC05-00OR22725.

References

Babu MM, Kriwacki RW, and Pappu RV (2012). Versatility from protein disorder. Science 337, 1460–1461. [PubMed: 22997313]

Beauchamp KA, Bowman GR, Lane TJ, Maibaum L, Haque IS, and Pande VS (2011). MSMBuilder2: Modeling Conformational Dynamics at the Picosecond to Millisecond Scale. J Chem Theory Comput 7, 3412–3419. [PubMed: 22125474]

Beautrait A, Paradis JS, Zimmerman B, Giubilaro J, Nikolajev L, Armando S, Kobayashi H, Yamani L, Namkung Y, Heydenreich FM, et al. (2017). A new inhibitor of the beta-arrestin/AP2 endocytic complex reveals interplay between GPCR internalization and signalling. Nat Commun 8, 15054. [PubMed: 28416805]

Benovic JL, Kuhn H, Weyand I, Codina J, Caron MG, and Lefkowitz RJ (1987). Functional desensitization of the isolated beta-adrenergic receptor by the beta-adrenergic receptor kinase: potential role of an analog of the retinal protein arrestin (48-kDa protein). Proc Natl Acad Sci U S A 84, 8879–8882. [PubMed: 2827157]

Best RB, Zhu X, Shim J, Lopes PE, Mittal J, Feig M, and Mackerell AD Jr. (2012). Optimization of the additive CHARMM all-atom protein force field targeting improved sampling of the backbone phi, psi and side-chain chi(1) and chi(2) dihedral angles. J Chem Theory Comput 8, 3257–3273. [PubMed: 23341755]

Betz RM Dabble (Version v2.6.3). Zenodo. 2017.

Bouzo-Lorenzo M, Santo-Zas I, Lodeiro M, Nogueiras R, Casanueva FF, Castro M, Pazos Y, Tobin AB, Butcher AJ, and Camina JP (2016). Distinct phosphorylation sites on the ghrelin receptor, GHSR1a, establish a code that determines the functions of ss-arrestins. Sci Rep 6, 22495. [PubMed: 26935831]

Busillo JM, Armando S, Sengupta R, Meucci O, Bouvier M, and Benovic JL (2010). Site-specific Phosphorylation of CXCR4 Is Dynamically Regulated by Multiple Kinases and Results in Differential Modulation of CXCR4 Signaling. J Biol Chem 285, 7805–7817. [PubMed: 20048153]

Butcher AJ, Prihandoko R, Kong KC, McWilliams P, Edwards JM, Bottrill A, Mistry S, and Tobin AB (2011). Differential G-protein-coupled receptor phosphorylation provides evidence for a signaling bar code. J Biol Chem 286, 11506–11518. [PubMed: 21177246]

Cahill TJ 3rd, Thomsen AR, Tarrasch JT, Plouffe B, Nguyen AH, Yang F, Huang LY, Kahsai AW, Bassoni DL, Gavino BJ, et al. (2017). Distinct conformations of GPCR-beta-arrestin complexes

mediate desensitization, signaling, and endocytosis. Proc Natl Acad Sci U S A 114, 2562–2567. [PubMed: 28223524]

Case DA, Ben-Shalom IY, Brozell SR, Cerutti DS, Cheatham TE III, Cruzeiro VWD, Darden TA, Duke RE, Ghoreishi D, Gilson MK, Gohlke H, Goetz AW, Greene D, Harris R, Homeyer N, Huang Y, Izadi S, Kovalenko A, Kurtzman T, Lee TS, LeGrand S, Li P, Lin C, Liu J, Luchko T, Luo R, Mermelstein DJ, Merz KM, Miao Y, Monard G, Nguyen C, Nguyen H, Omelyan I, Onufriev A, Pan F, Qi R, Roe DR, Roitberg AE, Sagui C, Schott-Verdugo S, Shen J, Simmerling CL, Smith JC, Salomon-Ferrer R, Swails JM, Walker RC, Wang J, Wei H, Wolf RM, Wu X, Xiao L, York DM and Kollman PA (2018). AMBER 2018. University of California, San Francisco.

Case DA, Cerutti DS, Cheatham TE III, Darden TA, Duke RE, Giese TJ, Gohlke H, Goetz AW, Greene D, Homeyer N, Izadi S, Kovalenko A, Lee TS, LeGrand S, Li P, Lin C, Liu J, Luchko T, Luo R, Mermelstein D, Merz KM, Monard G, Nguyen H, Omelyan I, Onufriev A, Pan F, Qi R, Roe DR, Roitberg A, Sagui C, Simmerling CL, Botello-Smith WM, Swails J, Walker RC, Wang J, Wolf RM, Wu X, Xiao L, York DM and Kollman PA (2017). AMBER 2017. University of California, San Francisco.

Coffa S, Breitman M, Hanson SM, Callaway K, Kook S, Dalby KN, and Gurevich VV (2011). The effect of arrestin conformation on the recruitment of c-Raf1, MEK1, and ERK1/2 activation. PLoS One 6, e28723.

Eichel K, Jullie D, Barsi-Rhyne B, Latorraca NR, Masureel M, Sibarita JB, Dror RO, and von Zastrow M. (2018). Catalytic activation of beta-arrestin by GPCRs. Nature 557, 381–386. [PubMed: 29720660]

Ghanouni P, Schambye H, Seifert R, Lee TW, Rasmussen SG, Gether U, and Kobilka BK (2000). The effect of pH on beta(2) adrenoceptor function. Evidence for protonation-dependent activation. J Biol Chem 275, 3121–3127. [PubMed: 10652295]

Gulbis JM, Kelman Z, Hurwitz J, O'Donnell M, and Kuriyan J. (1996). Structure of the C-terminal region of p21(WAF1/CIP1) complexed with human PCNA. Cell 87, 297–306. [PubMed: 8861913]

Gurevich VV, and Gurevich EV (2019). Plethora of functions packed into 45 kDa arrestins: biological implications and possible therapeutic strategies. Cell Mol Life Sci 76, 4413–4421. [PubMed: 31422444]

Han M, Gurevich VV, Vishnivetskiy SA, Sigler PB, and Schubert C. (2001). Crystal structure of beta-arrestin at 1.9 A: possible mechanism of receptor binding and membrane Translocation. Structure 9, 869–880. [PubMed: 11566136]

Hauser AS, Attwood MM, Rask-Andersen M, Schioth HB, and Gloriam DE (2017). Trends in GPCR drug discovery: new agents, targets and indications. Nat Rev Drug Discov 16, 829–842. [PubMed: 29075003]

Hirsch JA, Schubert C, Gurevich VV, and Sigler PB (1999). The 2.8 A crystal structure of visual arrestin: a model for arrestin's regulation. Cell 97, 257–269. [PubMed: 10219246]

Hopkins CW, Le Grand S, Walker RC, and Roitberg AE (2015). Long-Time-Step Molecular Dynamics through Hydrogen Mass Repartitioning. J Chem Theory Comput 11, 1864–1874. [PubMed: 26574392]

Huang J, and MacKerell AD Jr. (2013). CHARMM36 all-atom additive protein force field: validation based on comparison to NMR data. J Comput Chem 34, 2135–2145. [PubMed: 23832629]

Huang W, Masureel M, Qianhui Q, Janetzko J, Inoue A, Kato HE, Robertson MJ, Nguyen KC, Glenn JS, Skiniotis G, et al. (2020). Structure of the neurotensin receptor 1 in complex with beta-arrestin 1. Nature.

Humphrey W, Dalke A, and Schulten K. (1996). VMD: visual molecular dynamics. J Mol Graph 14, 33–38, 27–38. [PubMed: 8744570]

Hunter JD (2007). Matplotlib: A 2D Graphics Environment. Computing in Science & Engineering 9, 90–95.

Inagaki S, Ghirlando R, Vishnivetskiy SA, Homan KT, White JF, Tesmer JJ, Gurevich VV, and Grisshammer R. (2015). G Protein-Coupled Receptor Kinase 2 (GRK2) and 5 (GRK5) Exhibit Selective Phosphorylation of the Neurotensin Receptor in Vitro. Biochemistry 54, 4320–4329. [PubMed: 26120872]

Jacobson MP, Friesner RA, Xiang Z, and Honig B. (2002). On the role of the crystal environment in determining protein side-chain conformations. J Mol Biol 320, 597–608. [PubMed: 12096912]

Jacobson MP, Pincus DL, Rapp CS, Day TJ, Honig B, Shaw DE, and Friesner RA (2004). A hierarchical approach to all-atom protein loop prediction. Proteins 55, 351–367. [PubMed: 15048827]

Jung SR, Kushmerick C, Seo JB, Koh DS, and Hille B. (2017). Muscarinic receptor regulates extracellular signal regulated kinase by two modes of arrestin binding. Proc Natl Acad Sci U S A 114, E5579–E5588. [PubMed: 28652372]

Kim YJ, Hofmann KP, Ernst OP, Scheerer P, Choe HW, and Sommer ME (2013). Crystal structure of pre-activated arrestin p44. Nature 497, 142–146. [PubMed: 23604253]

Klauda JB, Venable RM, Freites JA, O'Connor JW, Tobias DJ, Mondragon-Ramirez C, Vorobyov I, MacKerell AD Jr., and Pastor RW (2010). Update of the CHARMM all-atom additive force field for lipids: validation on six lipid types. J Phys Chem B 114, 7830–7843. [PubMed: 20496934]

Kleiger G, Saha A, Lewis S, Kuhlman B, and Deshaies RJ (2009). Rapid E2-E3 assembly and disassembly enable processive ubiquitylation of cullin-RING ubiquitin ligase substrates. Cell 139, 957–968. [PubMed: 19945379]

Komolov KE, and Benovic JL (2018). G protein-coupled receptor kinases: Past, present and future. Cell Signal 41, 17–24. [PubMed: 28711719]

Latorraca NR, Wang JK, Bauer B, Townshend RJL, Hollingsworth SA, Olivieri JE, Xu HE, Sommer ME, and Dror RO (2018). Molecular mechanism of GPCR-mediated arrestin activation. Nature 557, 452–456. [PubMed: 29720655]

Lee MH, Appleton KM, Strungs EG, Kwon JY, Morinelli TA, Peterson YK, Laporte SA, and Luttrell LM (2016). The conformational signature of beta-arrestin2 predicts its trafficking and signalling functions. Nature 531, 665–668. [PubMed: 27007854]

Lohse MJ, and Hoffmann C. (2014). Arrestin interactions with G protein-coupled receptors. Handb Exp Pharmacol 219, 15–56. [PubMed: 24292823]

Lomize MA, Pogozheva ID, Joo H, Mosberg HI, and Lomize AL (2012). OPM database and PPM web server: resources for positioning of proteins in membranes. Nucleic Acids Res 40, D370–376. [PubMed: 21890895]

Luttrell LM, and Kenakin TP (2011). Refining efficacy: allosterism and bias in G protein-coupled receptor signaling. Methods Mol Biol 756, 3–35. [PubMed: 21870218]

MacKerell AD, Bashford D, Bellott M, Dunbrack RL, Evanseck JD, Field MJ, Fischer S, Gao J, Guo H, Ha S, et al. (1998). All-atom empirical potential for molecular modeling and dynamics studies of proteins. J Phys Chem B 102, 3586–3616. [PubMed: 24889800]

Maeda S, Qu Q, Robertson MJ, Skiniotis G, and Kobilka BK (2019). Structures of the M1 and M2 muscarinic acetylcholine receptor/G-protein complexes. Science 364, 552–557. [PubMed: 31073061]

Mann A, Liebetrau S, Klima M, Dasgupta P, Massotte D, and Schulz S. (2020). Agonist-induced phosphorylation bar code and differential post-activation signaling of the delta opioid receptor revealed by phosphosite-specific antibodies. Sci Rep 10, 8585. [PubMed: 32444688]

Mann A, Mouledous L, Froment C, O'Neill PR, Dasgupta P, Gunther T, Brunori G, Kieffer BL, Toll L, Bruchas MR, et al. (2019). Agonist-selective NOP receptor phosphorylation correlates in vitro and in vivo and reveals differential post-activation signaling by chemically diverse agonists. Sci Signal 12.

Mayer D, Damberger FF, Samarasimhareddy M, Feldmueller M, Vuckovic Z, Flock T, Bauer B, Mutt E, Zosel F, Allain FHT, et al. (2019). Distinct G protein-coupled receptor phosphorylation motifs modulate arrestin affinity and activation and global conformation. Nat Commun 10, 1261. [PubMed: 30890705]

Miess E, Gondin AB, Yousuf A, Steinborn R, Mosslein N, Yang Y, Goldner M, Ruland JG, Bunemann M, Krasel C, et al. (2018). Multisite phosphorylation is required for sustained interaction with GRKs and arrestins during rapid mu-opioid receptor desensitization. Sci Signal 11.

Milano SK, Pace HC, Kim YM, Brenner C, and Benovic JL (2002). Scaffolding functions of arrestin-2 revealed by crystal structure and mutagenesis. Biochemistry 41, 3321–3328. [PubMed: 11876640]

Mittag T, Marsh J, Grishaev A, Orlicky S, Lin H, Sicheri F, Tyers M, and Forman-Kay JD (2010). Structure/function implications in a dynamic complex of the intrinsically disordered Sic1 with the Cdc4 subunit of an SCF ubiquitin ligase. Structure 18, 494–506. [PubMed: 20399186]

Moerke NJ (2009). Fluorescence Polarization (FP) Assays for Monitoring Peptide-Protein or Nucleic Acid-Protein Binding. Curr Protoc Chem Biol 1, 1–15. [PubMed: 23839960]

Namkung Y, Le Gouill C, Lukashova V, Kobayashi H, Hogue M, Khoury E, Song M, Bouvier M, and Laporte SA (2016). Monitoring G protein-coupled receptor and beta-arrestin trafficking in live cells using enhanced bystander BRET. Nat Commun 7, 12178. [PubMed: 27397672]

Nishi H, Fong JH, Chang C, Teichmann SA, and Panchenko AR (2013). Regulation of protein-protein binding by coupling between phosphorylation and intrinsic disorder: analysis of human protein complexes. Molecular bioSystems 9, 1620–1626. [PubMed: 23364837]

Nobles KN, Xiao K, Ahn S, Shukla AK, Lam CM, Rajagopal S, Strachan RT, Huang TY, Bressler EA, Hara MR, et al. (2011). Distinct phosphorylation sites on the beta(2)-adrenergic receptor establish a barcode that encodes differential functions of beta-arrestin. Sci Signal 4, ra51.

Nuber S, Zabel U, Lorenz K, Nuber A, Milligan G, Tobin AB, Lohse MJ, and Hoffmann C. (2016). beta-Arrestin biosensors reveal a rapid, receptor-dependent activation/deactivation cycle. Nature 531, 661–664. [PubMed: 27007855]

Oakley RH, Laporte SA, Holt JA, Barak LS, and Caron MG (1999). Association of beta-arrestin with G protein-coupled receptors during clathrin-mediated endocytosis dictates the profile of receptor resensitization. J Biol Chem 274, 32248–32257. [PubMed: 10542263]

Park JY, Qu CX, Li RR, Yang F, Yu X, Tian ZM, Shen YM, Cai BY, Yun Y, Sun JP, et al. (2019). Structural Mechanism of the Arrestin-3/JNK3 Interaction. Structure 27, 1162–1170 e1163. [PubMed: 31080119]

Peterhans C, Lally CC, Ostermaier MK, Sommer ME, and Standfuss J. (2016). Functional map of arrestin binding to phosphorylated opsin, with and without agonist. Sci Rep 6, 28686. [PubMed: 27350090]

Peterson YK, and Luttrell LM (2017). The Diverse Roles of Arrestin Scaffolds in G Protein-Coupled Receptor Signaling. Pharmacol Rev 69, 256–297. [PubMed: 28626043]

Ranganathan A, Dror RO, and Carlsson J. (2014). Insights into the role of Asp79(2.50) in beta2 adrenergic receptor activation from molecular dynamics simulations. Biochemistry 53, 7283–7296. [PubMed: 25347607]

Roe DR, and Cheatham TE (2013a). PTRAJ and CPPTRAJ: Software for Processing and Analysis of Molecular Dynamics Trajectory Data. J Chem Theory Comput 9, 3084–3095. [PubMed: 26583988]

Roe DR, and Cheatham TE 3rd (2013b). PTRAJ and CPPTRAJ: Software for Processing and Analysis of Molecular Dynamics Trajectory Data. J Chem Theory Comput 9, 3084–3095. [PubMed: 26583988]

Rossi AM, and Taylor CW (2011). Analysis of protein-ligand interactions by fluorescence polarization. Nat Protoc 6, 365–387. [PubMed: 21372817]

Ryckaert J-P, Ciccotti G, and Berendsen HJ (1977). Numerical integration of the cartesian equations of motion of a system with constraints: molecular dynamics of n-alkanes. J Comp Phys 23, 327–341.

Salomon-Ferrer R, Gotz AW, Poole D, Le Grand S, and Walker RC (2013). Routine Microsecond Molecular Dynamics Simulations with AMBER on GPUs. 2. Explicit Solvent Particle Mesh Ewald. J Chem Theory Comput 9, 3878–3888. [PubMed: 26592383]

Sente A, Peer R, Srivastava A, Baidya M, Lesk AM, Balaji S, Shukla AK, Babu MM, and Flock T. (2018). Molecular mechanism of modulating arrestin conformation by GPCR phosphorylation. Nat Struct Mol Biol 25, 538–545. [PubMed: 29872229]

Shukla AK, Manglik A, Kruse AC, Xiao K, Reis RI, Tseng WC, Staus DP, Hilger D, Uysal S, Huang LY, et al. (2013). Structure of active beta-arrestin-1 bound to a G-protein-coupled receptor phosphopeptide. Nature 497, 137–141. [PubMed: 23604254]

Shukla AK, Westfield GH, Xiao K, Reis RI, Huang LY, Tripathi-Shukla P, Qian J, Li S, Blanc A, Oleskie AN, et al. (2014). Visualization of arrestin recruitment by a G-protein-coupled receptor. Nature 512, 218–222. [PubMed: 25043026]

Smith JS, and Rajagopal S. (2016). The beta-Arrestins: Multifunctional Regulators of G Protein-coupled Receptors. J Biol Chem 291, 8969–8977. [PubMed: 26984408]

Sommer ME, Hofmann KP, and Heck M. (2012). Distinct loops in arrestin differentially regulate ligand binding within the GPCR opsin. Nat Commun 3, 995. [PubMed: 22871814]

Staus DP, Hu H, Robertson MJ, Kleinhenz ALW, Wingler LM, Capel WD, Latorraca NR, Lefkowitz RJ, and Skiniotis G. (2020). Structure of the M2 muscarinic receptor-beta-arrestin complex in a lipid nanodisc. Nature 579, 297–302. [PubMed: 31945772]

Tian X, Kang DS, and Benovic JL (2014). beta-arrestins and G protein-coupled receptor trafficking. Handb Exp Pharmacol 219, 173–186. [PubMed: 24292830]

Tobin AB (2008). G-protein-coupled receptor phosphorylation: where, when and by whom. Br J Pharmacol 153 Suppl 1, S167–176. [PubMed: 18193069]

Vanommeslaeghe K, Hatcher E, Acharya C, Kundu S, Zhong S, Shim J, Darian E, Guvench O, Lopes P, Vorobyov I, et al. (2010). CHARMM general force field: A force field for drug-like molecules compatible with the CHARMM all-atom additive biological force fields. J Comput Chem 31, 671–690. [PubMed: 19575467]

Vanommeslaeghe K, and MacKerell AD Jr. (2012). Automation of the CHARMM General Force Field (CGenFF) I: bond perception and atom typing. J Chem Inf Model 52, 3144–3154. [PubMed: 23146088]

Vanommeslaeghe K, Raman EP, and MacKerell AD Jr. (2012). Automation of the CHARMM General Force Field (CGenFF) II: assignment of bonded parameters and partial atomic charges. J Chem Inf Model 52, 3155–3168. [PubMed: 23145473]

Verweij EWE, Al Araaj B, Prabhata WR, Prihandoko R, Nijmeijer S, Tobin AB, Leurs R, and Vischer HF (2020). Differential Role of Serines and Threonines in Intracellular Loop 3 and C-Terminal Tail of the Histamine H4 Receptor in beta-Arrestin and G Protein-Coupled Receptor Kinase Interaction, Internalization, and Signaling. ACS pharmacology & translational science 3, 321–333. [PubMed: 32296771]

Webb B, and Sali A. (2014). Protein structure modeling with MODELLER. Methods Mol Biol 1137, 1–15. [PubMed: 24573470]

Xiao K, McClatchy DB, Shukla AK, Zhao Y, Chen M, Shenoy SK, Yates JR 3rd, and Lefkowitz RJ (2007). Functional specialization of beta-arrestin interactions revealed by proteomic analysis. Proc Natl Acad Sci U S A 104, 12011–12016. [PubMed: 17620599]

Yang F, Xiao P, Qu CX, Liu Q, Wang LY, Liu ZX, He QT, Liu C, Xu JY, Li RR, et al. (2018). Allosteric mechanisms underlie GPCR signaling to SH3-domain proteins through arrestin. Nat Chem Biol 14, 876–886. [PubMed: 30120361]

Yang F, Yu X, Liu C, Qu CX, Gong Z, Liu HD, Li FH, Wang HM, He DF, Yi F, et al. (2015). Phospho-selective mechanisms of arrestin conformations and functions revealed by unnatural amino acid incorporation and (19)F-NMR. Nat Commun 6, 8202. [PubMed: 26347956]

Yang Z, Yang F, Zhang D, Liu Z, Lin A, Liu C, Xiao P, Yu X, and Sun JP (2017). Phosphorylation of G Protein-Coupled Receptors: From the Barcode Hypothesis to the Flute Model. Mol Pharmacol 92, 201–210. [PubMed: 28246190]

Zhang L, and Hermans J. (1996). Hydrophilicity of cavities in proteins. Proteins 24, 433–438. [PubMed: 9162944]

Zhou XE, He Y, de Waal PW, Gao X, Kang Y, Van Eps N, Yin Y, Pal K, Goswami D, White TA, et al. (2017). Identification of Phosphorylation Codes for Arrestin Recruitment by G Protein-Coupled Receptors. Cell 170, 457–469 e413. [PubMed: 28753425]

Zhuo Y, Gurevich VV, Vishnivetskiy SA, Klug CS, and Marchese A. (2020). A non-GPCR binding partner interacts with a novel surface on beta-arrestin1 to mediate GPCR signaling. J Biol Chem.

Zhuo Y, Vishnivetskiy SA, Zhan X, Gurevich VV, and Klug CS (2014). Identification of receptor binding-induced conformational changes in non-visual arrestins. J Biol Chem 289, 20991–21002. [PubMed: 24867953]

Highlights:

- MD simulations and spectroscopy monitor β-arrestin as GPCR phosphorylation varies
- Phosphate locations affect arrestin activation and binding strongly but differently
- Different GPCR phosphorylation patterns favor different arrestin conformations
- Phosphate-dependent conformations may select among diverse arrestin functions

Arrestin-GPCR interactions lead to a range of signaling outputs that can be independently tuned through adjustments in the phosphorylation pattern of the receptor.

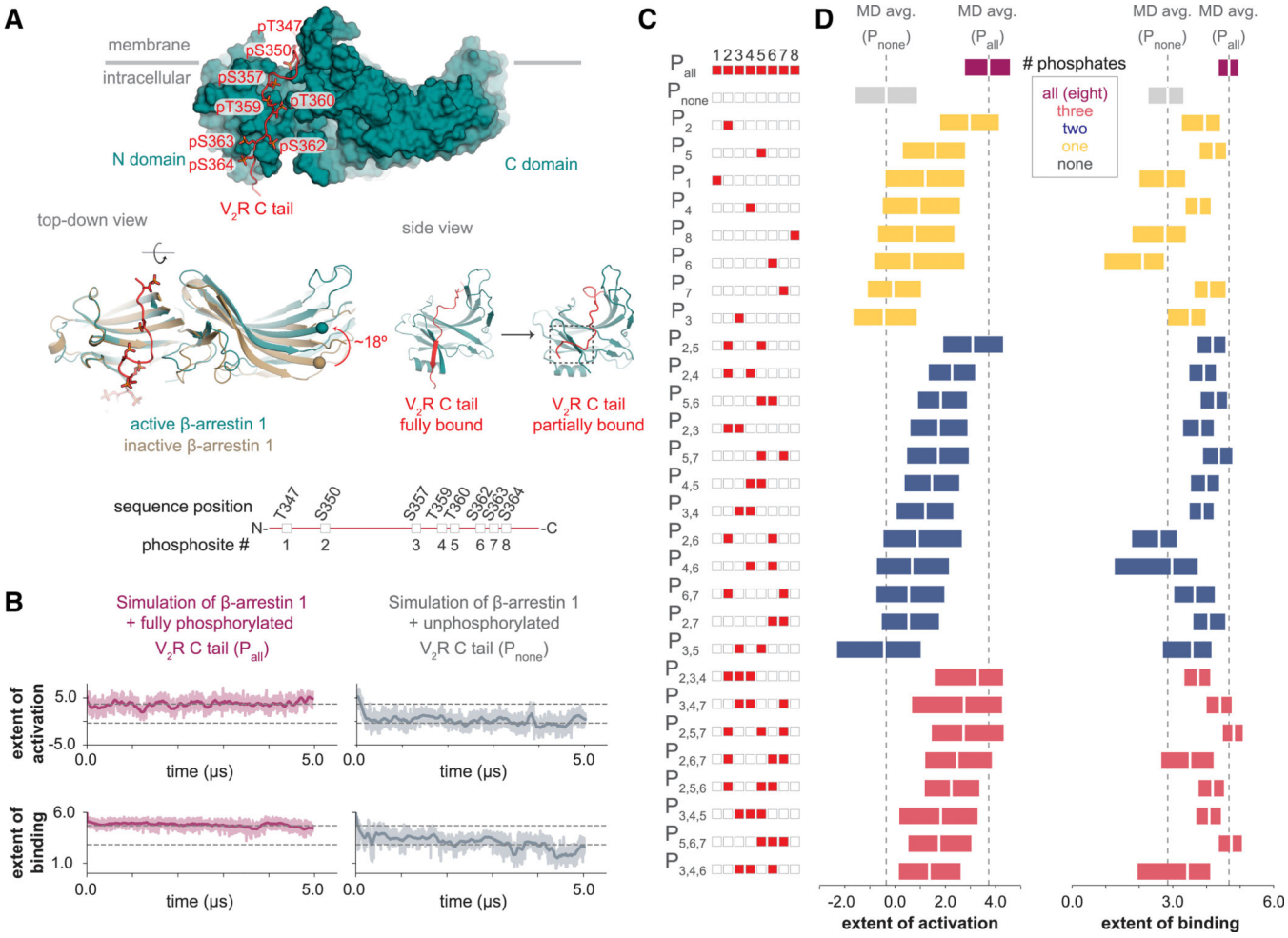

Figure 1. Phosphorylation patterns that promote arrestin activation differ from those that favor arrestin binding.

A Top: Crystal structure of β-arrestin 1 (teal) bound to the fully phosphorylated V_2R C-tail (P_{all}, red). Middle: Compared to the inactive-state structure (tan), the C domain of arrestin twists relative to the N domain upon activation; we monitor this large-scale conformational change (left), as well as the binding stability of the V_2R C tail (right), in simulation (see Methods). Bottom: numbering of phosphorylation sites on the V_2R C-tail. **B** Top: Arrestin stays close to its initial active conformation in simulations of β-arrestin 1 bound to P_{all} but quickly relaxes to inactive-like conformations when all phosphates are removed from the V_2R C-tail (P_{none}). Bottom: P_{all} remains stably bound but P_{none} does not. Thick traces represent 50-ns moving averages; thin traces represent unsmoothed values. Dashed lines correspond to the simulation average for the fully phosphorylated condition (upper line) and the unphosphorylated condition (lower line). **C** Phosphorylation patterns of the V_2R C-tail used in simulations. **D** Extent of activation (left) and strength of binding (right) for simulations with each phosphorylation pattern. Depending on phosphate locations, peptides with equal numbers of phosphates can stabilize arrestin's active state no more than P_{none} or nearly as much P_{all}; the same is true for effects on arrestin binding. Box plots show 25th, 50th and 75th percentiles of each distribution. See also Figure S1-S3.

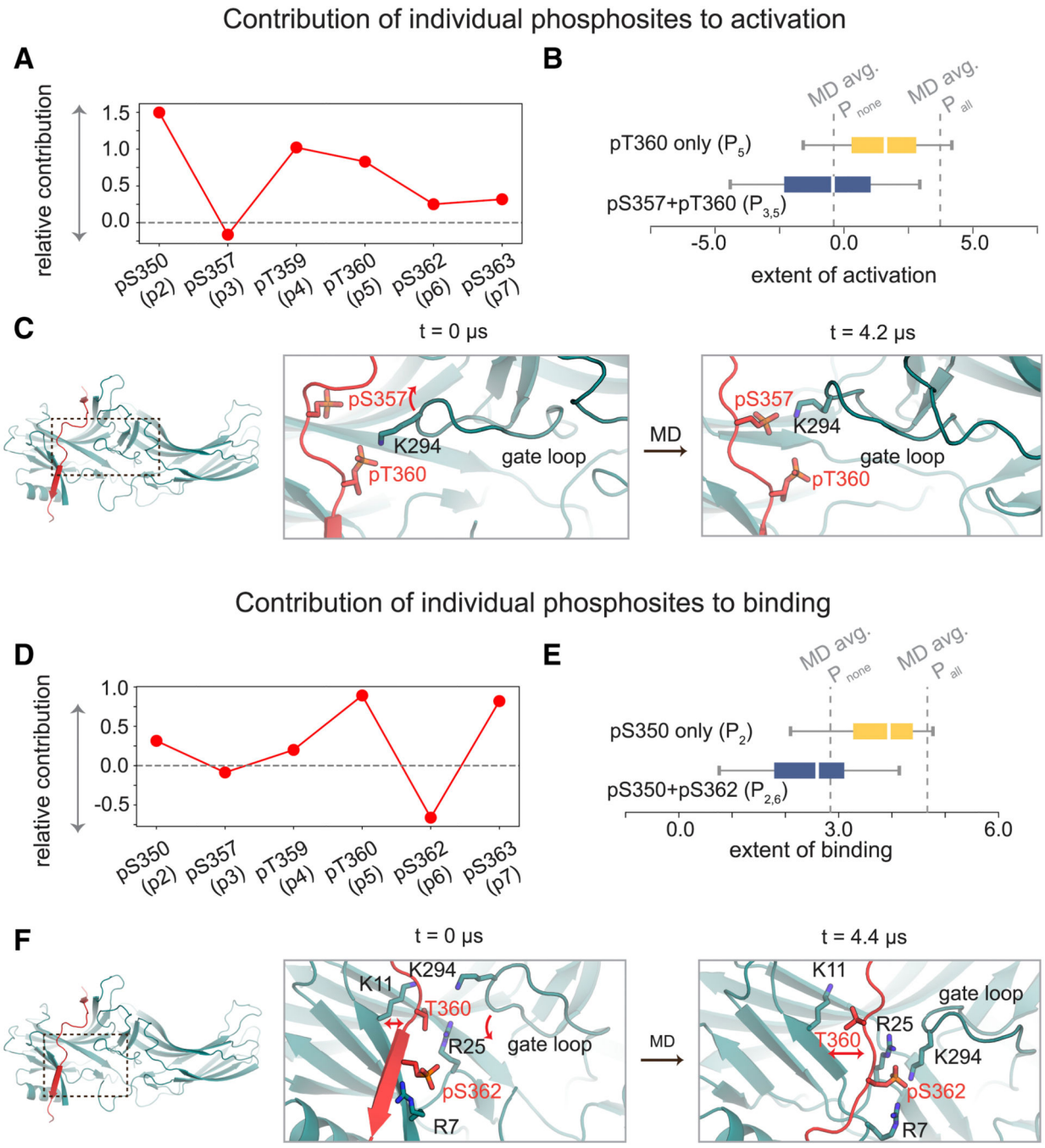

Figure 2. Phosphates at different sites vary widely in their tendency to stimulate or inhibit arrestin activation and binding.

Typical contributions of phosphate addition at each site to activation (**A**) and binding strength (**D**). A positive value indicates that phosphate addition at a given site typically promotes activation/binding, and a negative value indicates that phosphate addition typically inhibits activation/binding, but the effect of phosphorylating a particular site can vary substantially depending on which other sites are phosphorylated. **B** Adding phosphate pS357 to a peptide phosphorylated at T360 substantially reduces arrestin activation; **C** K294 of

arrestin's gate loop moves away from pT360 to engage pS357, hindering the interdomain twisting motion associated with activation. **E** Adding pS362 to a peptide phosphorylated at S350 substantially reduces binding; **F** K294 swings down to engage pS362, causing rearrangement of a polar network near the tail-binding interface and thus disrupting interactions between the arrestin N terminus and the V_2R C-tail. Whiskers in box plots represent the 5^{th} and 95^{th} percentiles of the distributions for each simulation condition. See also Figure S1–S3.

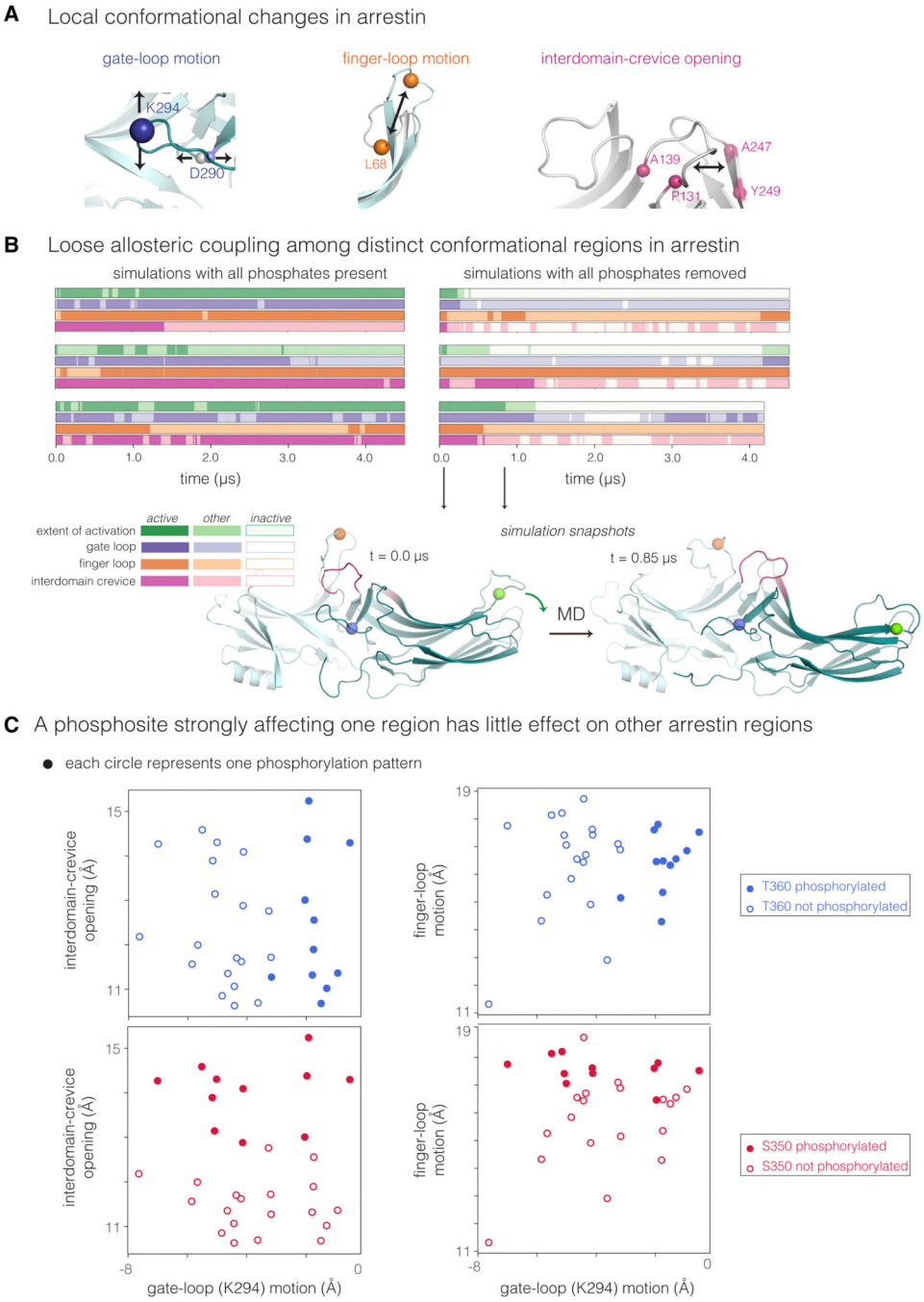

Figure 3. Different regions of arrestin can change conformation independently.

A Local conformational changes and metrics used to quantify them (see Methods). **B** Each bar shows the conformational state of one arrestin region over the course of a simulation, with dark colors representing conformations close to the active structure, and white representing conformations close to inactive structures. Three representative simulations with P_{all} (left) or P_{none} (right) bound. Even when arrestin adopts active-like global conformations, local regions may remain in inactive-like conformations. In the simulation snapshot at right, the interdomain crevice (pink) has collapsed to an inactive-like

conformation, even as the global conformation of arrestin and the gate loop conformation remain active-like; the finger loop adopts an intermediate conformation. **C** Phosphorylation at certain sites affects conformations of some regions but not others. Phosphorylation at T360 substantially affects gate loop conformation, whereas phosphorylation at S350 substantially affects finger loop and interdomain crevice conformations. In each plot, each circle represents one phosphorylation pattern; its coordinates represent median values for simulations with that phosphorylation pattern. See also Figure S4.

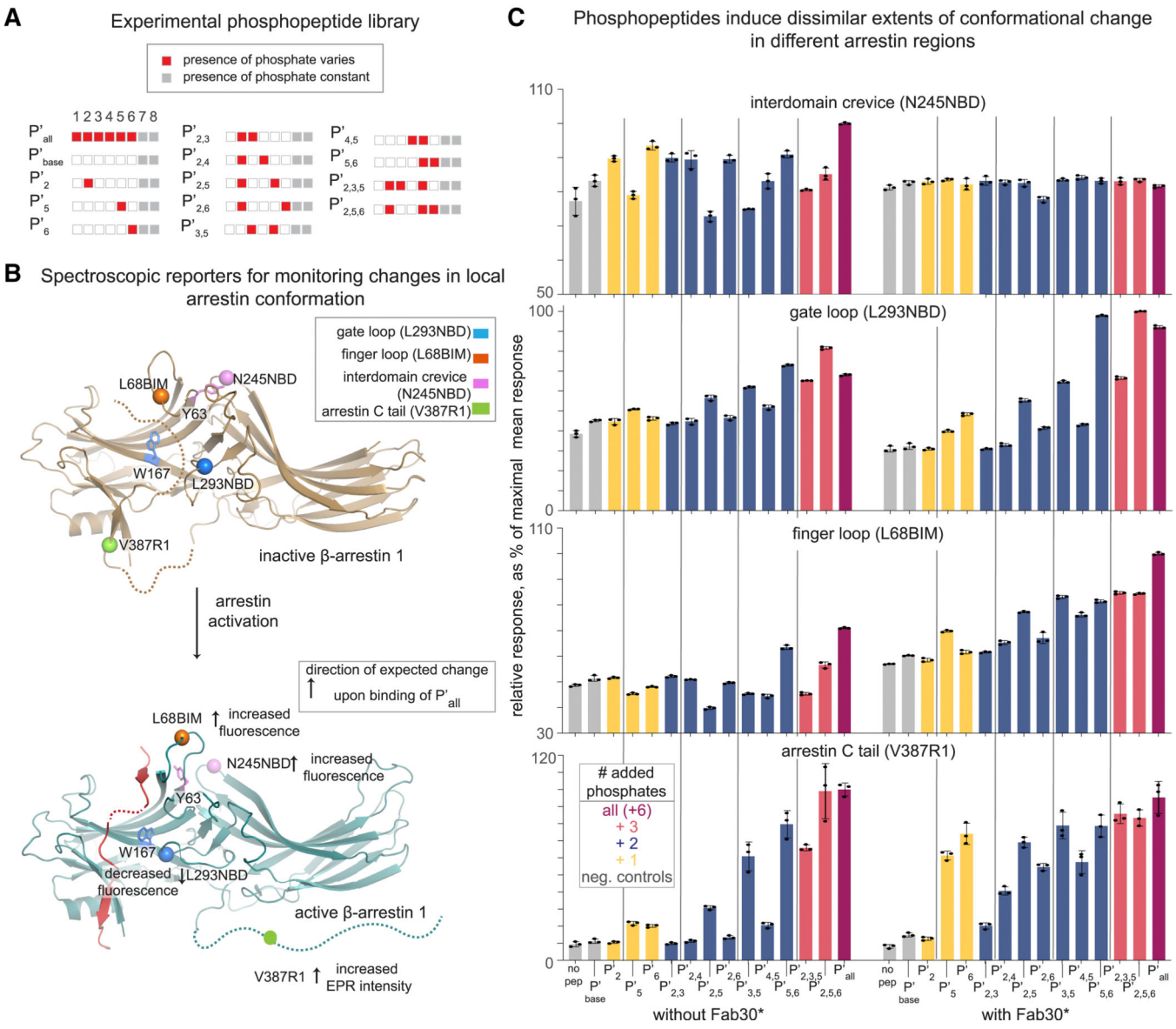

Figure 4. Site-directed spectroscopy supports computational findings.

A Phosphopeptides used in site-directed spectroscopy experiments. **B** Locations of spectroscopic reporters designed to monitor conformational changes. Fluorescent reporters monitor the conformations of the finger loop, interdomain crevice and gate loop. Fluorescence intensity decreases with solvent exposure and with proximity to tyrosine and tryptophan residues. A spin label at the proximal end of the arrestin C tail allows EPR spectroscopy to monitor mobility of this site, as indicated by increased intensity of the left-field peak. **C** Phosphopeptides with the same number of phosphates vary substantially in ability to elicit conformational responses at each of these four regions. An active-state-stabilizing antibody fragment, Fab30*, prevents phosphopeptides from altering the conformation of the interdomain crevice (top right), but phosphopeptides still modulate the conformation of the arrestin gate loop, finger loop, and C tail. Error bars represent standard deviation of three replicates. See also Figure S5.

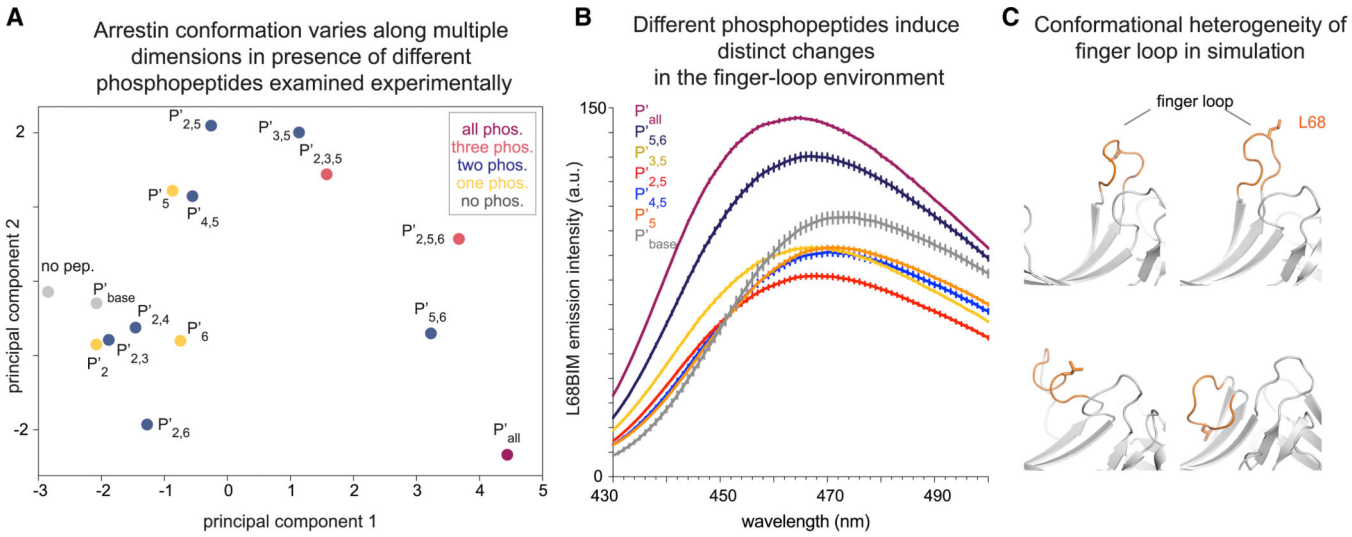

Figure 5. Phosphopeptides select among diverse arrestin conformations.

A Principal components analysis of experimental responses to different phosphopeptides. The first component captures major global rearrangements associated with the inactive-to-active transition, such that the minimally phosphorylated and fully phosphorylated peptides adopt near-minimal and maximal values, respectively. The other components, which account for 40% of the overall variance in experimental responses, capture conformational changes that are orthogonal to, and not correlated with, the first component. **B** Fluorescence emission spectra for the finger loop reveal that phosphopeptides modulate both the amplitude (i.e. extent of solvent exposure) and the wavelength (i.e. polarity of the local chemical environment) of the labeled site and show that the finger loop can undergo multiple conformational changes in the presence of phosphopeptide. **C** In simulation, the finger loop (orange) also adopts multiple distinct conformations. See also Figure S5.

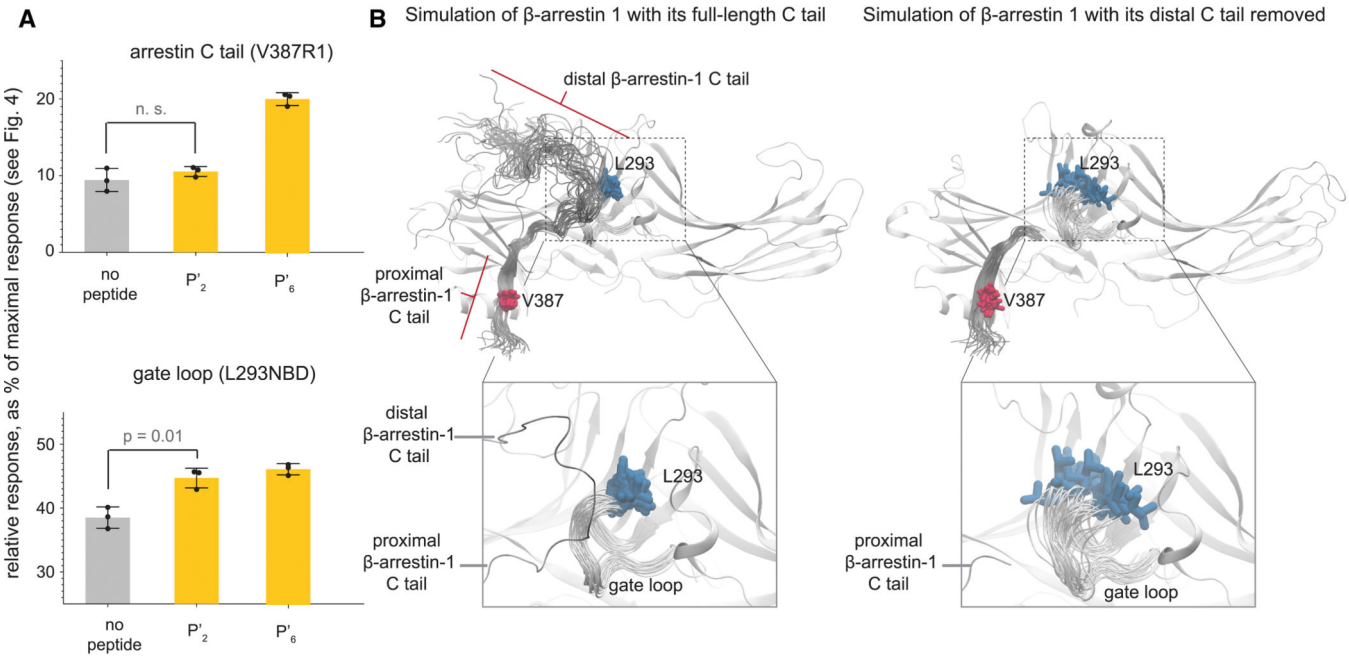

Figure 6. Phosphopeptides can trigger conformational changes in arrestin without fully displacing the arrestin C tail.

A Certain peptides (e.g., P'$_2$) promote conformational changes in the gate loop (bottom) without triggering full release of the arrestin C tail (top). **B** In simulation, the distal arrestin C tail is fairly disordered and occasionally unbinds, revealing an empty groove on the arrestin N domain to which a phosphopeptide could then bind. Right: When the distal portion of the arrestin C tail is removed, the gate loop becomes more mobile, in agreement with the experimental observation that a phosphopeptide need not fully displace the arrestin C tail to cause conformational changes in arrestin. Each image shows snapshots sampled every 100 ns during 3.1 μs of simulation. See also Figure S6.

Key Resources Table

REAGENT or RESOURCE	SOURCE	IDENTIFIER
Bacterial and Virus Strains		
E. coli NiCo21(DE3)	NEB	Cat# C2529H
E. coli Rosetta (DE3)	Millipore Sigma	Cat# 70954–3
Chemicals, Peptides, and Recombinant Proteins		
P'_{base}	Tufts University Core facility	N/A
P'_{2}	Tufts University Core facility	N/A
P'_{5}	Tufts University Core facility	N/A
P'_{6}	Tufts University Core facility	N/A
$P'_{2,3}$	Tufts University Core facility	N/A
$P'_{2,4}$	Tufts University Core facility	N/A
$P'_{2,5}$	Tufts University Core facility	N/A
$P'_{2,6}$	Tufts University Core facility	N/A
$P'_{3,5}$	Tufts University Core facility	N/A
$P'_{4,5}$	Tufts University Core facility	N/A
$P'_{5,6}$	Tufts University Core facility	N/A
$P'_{2,3,5}$	Tufts University Core facility	N/A
$P'_{2,5,6}$	Tufts University Core facility	N/A
P'_{all}	Tufts University Core facility	N/A
FITC-P'_{all}	Tufts University Core facility	N/A
monobromobimane	Thermo Fisher Scientific	Cat# M1378
IANBD	Thermo Fisher Scientific	Cat# D2004
MTSSL	Enzo Life Sciences	Cat# ALX-430–134
DTNB	Thermo Fisher Scientific	Cat# 22582
L-Cysteine	Sigma-Aldrich	Cat# 30089
Coelenterazine 400a	Nanolight Technology	Cat# 340
Anti-SNAP antibody	GenScript	Cat# A00684
Anti-rabbit HRP antibody	GE Healthcare	N/A
SigmaFast OPD tablets	Sigma-Aldrich	Cat# P9187
Dulbecco's Modified Eagle's Medium	Wisent Bio Products	Cat# 319–051-CL Cat# 319–050-CL

REAGENT or RESOURCE	SOURCE	IDENTIFIER
Newborn Calf Serum	Wisent Bio Products	Cat# 075–150
Polyethylenimine, linear, 25 kDa	Polysciences	Cat# 23966–1
[Arg8]-vasopressin	Genemed Synthesis Inc.	Cat# SP-89700–5
Coelenterazine 400a	NanoLight Technology	Cat# 340
Deposited Data		
Site-directed fluorescence spectroscopy, EPR spectroscopy and BRET biosensor data	This paper; Mendeley Data	http://dx.doi.org/10.17632/nvwjmnsnjp.1
Molecular dynamics simulation data	This paper; Zenodo	http://dx.doi.org/10.5281/zenodo.3991060
Active-state crystal structure of β-arrestin 1 bound to the phosphorylated V_2R C-tail and Fab30	Shukla et al., 2013	PDB: 4JQI
Inactive-state crystal structure of β-arrestin 1	Han et al., 2001	PDB: 1G4M
Inactive-state crystal structure of β-arrestin 1	Milano et al., 2002	PDB: 1JSY
Cryo-EM structure of β-arrestin 1 bound to M2 muscarinic acetylcholine receptor ligated to the V2R C-tail (M_2V_2R)	Staus et al., 2020	PDB: 6U1N
Cryo-EM structure of Go bound to M_2R	Maeda et al., 2019	PDB: 6OIK
Inactive-state crystal structure of visual arrestin	Hirsch et al., 1999	PDB: 1CF1
Experimental Models: Cell Lines		
Human embryonic kidney (HEK293 SL) cells	(Beautrait et al., 2017)	Gift from laboratory of Stéphane Laporte
Oligonucleotides		
bArr1 L68C Fw primer gaatgtcaagcccaaaacatcgcagtcttcgcgtccatagcgaaa	Stanford PAN facility	N/A
bArr1 L68C Rv primer tttcgctatggacgcgaagactgcgatgttttgggcttgacattc	Stanford PAN facility	N/A
bArr1 V167W Fw primer gggcgtattgaactttgcgaatccacagacggacggaattacgtttg	Stanford PAN facility	N/A
bArr1 V167W Rv primer caaacgtaattccgtccgtctgtggattcgcaaagttcaatacgccc	Stanford PAN facility	N/A
bArr1 L293C Fw primer aaattagtgtcctcgtgcttgcatttcccgtccagcgctaaaccg	Stanford PAN facility	N/A
bArr1 L293C Rv primer cggtttagcgctggacgggaaatgcaagcacgaggacactaattt	Stanford PAN facility	N/A
bArr1 N245C Fw primer gaccttgtactgagctgtgcagaagagaacgatgtctgca	Stanford PAN facility	N/A
bArr1 N245C Rv primer tgcagacatcgttctcttctgcacagctcagtacaaggtc	Stanford PAN facility	N/A
bArr1 V387C Fw primer ggcgtgcaaagtcctcgaagcagatatcatcatcattagtatctaa	Stanford PAN facility	N/A
bArr1 V387C Rv primer ttagatactaatgatgatgatatctgcttcgaggactttgcacgcc	Stanford PAN facility	N/A
Recombinant DNA		
pMAL-scdsFv30	This study	N/A
pET15b-bArr1L68C	This study	N/A
pET15b-bArr1V167W/L293C	This study	N/A
pET15b-bArr1N245C	This study	N/A
pET15b-bArr1V387C	This study	N/A

REAGENT or RESOURCE	SOURCE	IDENTIFIER
pcDNA4/TO-V2R P_{all}	This study	N/A
pcDNA4/TO-V2R P_{none}	This study	N/A
pcDNA4/TO-V2R $P_{2,5,7}$	This study	N/A
pcDNA4/TO-V2R $P_{2,5,6}$	This study	N/A
pcDNA4/TO-V2R $P_{5,7}$	This study	N/A
pcDNA4/TO-V2R $P_{2,6}$	This study	N/A
pcDNA3.1-βarr1-RlucII	(Namkung et al., 2016)	N/A
pcDNA3.1-rGFP-CAAX	(Namkung et al., 2016)	N/A
Software and Algorithms		
FluorEssence v3.8	Horiba, Inc.	www.horiba.com
GraphPad Prism 7.0, 8.0	GraphPad, Inc.	https://www.graphpad.com/scientific-software/prism/
PyMOL	Schrödinger, Inc.	https://www.pymol.org
Prime	Schrödinger, Inc.	https://www.schrodinger.com/prime
Maestro	Schrödinger, Inc.	https://www.schrodinger.com/maestro
Dabble	(Betz, 2017)	http://dabble.robinbetz.com/
Dowser	(Zhang, 1996)	http://danger.med.unc.edu/hermans/dowser/dowser.htm or https://web.archive.org/web/20100614150432/http://hekto.med.unc.edu:8080/HERMANS/software/DOWSER/dowser.tar.gz
AMBER16 and AMBER17	(Case, 2017)	http://ambermd.org/
CPPTRAJ	(Roe and Cheatham, 2013a)	http://ambermd.org/
VMD	(Humphrey et al., 1996)	http://www.ks.uiuc.edu/Research/vmd/
Matplotlib	(Hunter, 2007)	http://matplotlib.org/1.2.1/index.html
Rosetta FloppyTail	(Kleiger et al., 2009)	http://rosettacommons.org/docs/latest/application_documentation/structure_prediction/floppy-tail